AN ABSTRACT OF THE THESIS OF

Supriya V. Pawar, for the degree of Master of Science in Industrial Engineering, presented on March 21, 2013

Title: Fabrication of Precipitation-Hardened Aluminum Microchannel Cooling Plates for Adsorption-Based Hydrogen Storage Systems

Abstract Approved: _____

Brian K. Paul

The need for clean and renewable fuel such as hydrogen is driven by a growing worldwide population and increasing air pollution from fossil fuels. One of the major barriers for the use of hydrogen in automotive industry is the storage of hydrogen. Physisorption is the most promising storage technique due to its high storage density, reversibility and rapid sorption kinetics besides being safe and volume-efficient. A major challenge for physisorption is the need to manage the heat of adsorption at cryogenic temperatures. In this thesis, a 6061 aluminum microchannel cooling plate is designed to remove the equivalent heat flux required by the adsorption of hydrogen within an adsorption bed. Therefore, the objective of this thesis is to determine whether laser welding and heat treating strategies can be developed for a 6061

aluminum microchannel cooling plate as part of a larger hydrogen storage thermal management system. Key manufacturing process requirements include controlling the hermeticity, strength and dimensional stability of the heat-treated weld joint. A hermetic microchannel cooling plate was successfully laser welded and heat treated using free convection in air to quench the solution heat treatment. The weld strength and warpage obtained were within acceptable limits. Experimental testing of the fabricated microchannel cooling plate showed acceptable percent error with an experimental heat removal rate within 13.4% of computational fluid dynamics (CFD) analyses and an average pressure drop error of 25%. Calculations show that the cooling plate developed could support a hydrogen storage thermal management system taking up 5.0% and 10.3% of the system displacement volume and mass, respectively.

Fabrication of Precipitation-Hardened Aluminum Microchannel Cooling Plates for Adsorption-Based Hydrogen Storage Systems

by

Supriya V. Pawar

A THESIS

Submitted to

Oregon State University

in partial fulfillment of

the requirements for the

degree of

Master of Science

Presented March 21, 2013

Commencement June 2013

Master of Science thesis of Supriya V. Pawar presented on March 21, 2013.

APPROVED:

_____

Major Professor, representing Industrial Engineering

_____

Head of the School of Mechanical, Industrial, and Manufacturing Engineering

_____

Dean of the Graduate School

I understand that my thesis will become a part of the permanent collection of the Oregon State University libraries. My signature below authorizes release of my thesis to any reader upon request.

_____

Supriya V. Pawar, Author

ACKNOWLEDGEMENTS

First and foremost, I would like to express my sincere gratitude to my advisor, Professor Brian K. Paul, for giving me the opportunity to pursue my master degree at Oregon State University under his precious guidance. His continual support, guidance and advice he gave me during my graduate study enabled me to complete my master's thesis. I would like to specially thank Dr. Kevin Drost, Dr. David Kim and Dr. Scott Leavengood for their valuable advice and time.

I would like to thank Dr. Frank Tepley, Teresa Sawyer, Steve Etringer, for their assistance with EPMA, SEM tests and machining respectively. I would also like to thank Dr Vinod Narayanan and Erfan Rasouli for letting me use their test setup for my experiments. I would like to thank Daniel Peterson and Eric Truong for their help with the CFD analysis.

I would like to extend my appreciation to all the members at Micro Breakthrough Institute (MBI), Don Higgins, Jair Lizarazo, Jack Rundel, Hailei Wang, Neill Thornton, Sudhir Ramprasad, Thomas Lindner etc. for their valuable assistance and time.

I would also like to thank my fellow graduate students, Babak Lajevardi, Barath Palanisamy, Clayton Hires, Leif Steigleder, Ravi Eluri, Sam Brannon, and all other friends at OSU for their encouragement and assistance and making my experience of studying abroad enjoyable.

Most of all, I would like to express my love and gratitude to my family and friends for their endless support in all aspects of my life.

CONTRIBUTION OF AUTHORS

Dr. Vinod Narayanan and Erfan Rasouli for help with test setup for functional analysis.

Daniel Peterson and Eric Truong for the assistance with theoretical analysis of cooling plate with CFD simulation.

TABLE OF CONTENTS

TABLE OF CONTENTS (Continued)

LIST OF FIGURES

LIST OF FIGURES (Continued)

LIST OF TABLES

Fabrication of Precipitation-Hardened Aluminum Microchannel Cooling Plates for Adsorption-Based Hydrogen Storage Systems

1. Introduction

Interest in hydrogen as a fuel exists due to the increasing demand of energy caused by an increasing world population and the desire to reduce fossil fuel usage. The US Geological Survey estimates that while one half of all oil reserves are undiscovered, one half of the discovered supplies are already consumed. [1] The growth of the global economy and resulting increase in motorized transportation is putting heightened demand on the world's remaining oil reserves. Approximately two-thirds of increased oil demand is expected to be in the transportation sector which includes light duty vehicles and other transportation like air, rail etc. [3] Combine this with political instabilities in regions with the highest oil reserves and oil prices are expected to continue to increase over the next decade [2, 3]. This is a big concern for the US which has small quantities of oil reserves and more than 50% of oil demand fulfilled by imported oil.

Other concerns with fossils fuels include the air pollution caused by the combustion of fossil fuels. More than 60% of Americans live in areas where the level of one or more pollutants is high enough to affect public health and the environment. [4] Personal vehicles and electric power plants are significant contributors to the pollution. Hence, improving US energy security requires attention to environmental concerns as well. Strategies include improving the energy efficiency of the

transportation system while developing domestic and clean, non-petroleum fuels. [2, 3]

Hydrogen is the cleanest fuel and has a heating value three times higher than that of gasoline. It stores and delivers energy with zero or near zero emissions depending upon how it is used. Fuel cell-based stationary power generation from hydrogen is clean and quiet. Hydrogen is not available naturally and so requires energy to synthesize it from diverse domestic resources including fossils fuels, natural gas, or biomass using various sources of power including nuclear, wind, solar, geothermal or hydroelectric. The synthesis of hydrogen using electricity or renewable resources is a form of energy storage which can be helpful when power generation is high and demand is low. [5, 6, 7]

Fuel cells or other power cycles can be used to convert hydrogen back to electricity when needed. For motive power systems, polymer electrolyte membrane (PEM) fuel cells can be used to extract power from hydrogen. In transit buses, fuel cell efficiencies can be more than 40% and 50% compared with diesel internal combustion engines (ICE) and natural gas ICEs, respectively. In light duty vehicles, fuel cell efficiencies are more than 53 and 59% higher compared with gasoline ICE and hybrid electric power engines, respectively. [5, 6, 7] A life-cycle emissions model developed by Argonne National Laboratory indicates that fuel cell-based power leads to a reduction in greenhouse gases and pollutants by 40% over gasoline ICEs, by 15% over gasoline hybrid electric vehicles, and 25% over gasoline powered plug-in hybrids. [5, 6, 7]Besides energy security and environmental concerns, the fast

adoption of highly efficient fuel cell-based power systems is expected to lead USA to competitive advantage.

In order to achieve commercialization of fuel cells, several technical challenges need to be addressed. The bottleneck in the use of hydrogen within light duty vehicles is the on-board storage of hydrogen. The development of safe, reliable, compact and cost effective hydrogen storage on-board vehicles is technically challenging.

1.1 Hydrogen storage

Hydrogen is a promising fuel with three times the energy content of gasoline by weight. However, the energy content of hydrogen by volume is approximately four times less than that of gasoline [9]. At standard temperature and pressure, the volume required to store one kg of hydrogen is 11 m^3.[11] Approximately 5.6 kg of hydrogen is required to provide energy for a driving range of 300 miles, generally regarded as the minimum range for widespread public acceptance. Thus, a hydrogen storage tank 61.6 m^3 in volume is required on-board the vehicle which is larger than most cars by itself.

Through its Hydrogen Storage Engineering Center of Excellence, the US Department of Energy (DOE) has developed hydrogen storage performance goals for light duty vehicles. [11] The short term goals for 2017 consists of obtaining a gravimetric density of 5.5 wt% (1.8 kWh/kg) and a volumetric density of 0.04 kg hydrogen/L (1.3 kWh/L) for on-board hydrogen storage necessary to drive 300 miles.

A complete list of the short term and long term goals for on-board hydrogen storage can be obtained in Appendix A. [11]

Several methods are available for hydrogen storage including compression, liquefaction, cryo-compression, metallic hydrides and complex hydrides, and physisorption. [9, 10, 12] Compressed hydrogen is the simplest method to store hydrogen in cylinders but the energy density obtained is very low. A technical assessment of 350 and 700 bar compressed tank systems showed that at room temperature, the compressed storage capacity obtained does not fulfill the DOE targets. Also, safety is a big concern associated with high pressure hydrogen tanks. [13, 14]

Liquid hydrogen can be stored at atmospheric pressure in cryogenic tanks at 21.2 K. The volumetric density obtained is 70.8 g/L which is twice the compressed hydrogen at 700 bar. The technical energy required to liquefy hydrogen from room temperature is approximately 15.2 kWh/kg, which is almost half of the lower heat value (LHV) of hydrogen combustion. [15, 16] In addition to the high energy consumption required during liquefaction, the continuous boil-off (emission of H2 into the atmosphere) of hydrogen during storage limits the application of this storage method for on-board storage in light duty vehicles. [16]

Cryo-compression is another storage method in which hydrogen is compressed at liquid nitrogen temperatures and moderate pressures e.g. 150 bars. [17] This manner of storage addresses most of the short-comings of the (Liquid hydrogen) LH_2 strategy and meets all 2015 storage targets except cost and efficiency. The cost associated with manufacturing these systems is two to three times the DOE targets. [14, 18]

Compared to previous methods, metal hydrides and complex hydrides offer a safe and efficient way to store hydrogen. [15] Many metals and alloys react with hydrogen to form hydrides. The charging process releases heat while the discharging process requires heat. Hydrogen storage in metal hydrides can be grouped into roughly two groups. Low temperature hydrides release hydrogen at Standard temperature and pressure (STP), but the gravimetric capacities of these hydrides are low e.g. < 2 wt%. Examples include FeTiH1:8 and LaNi5H6.[9,12] High temperature hydrides provide gravimetric capacities up to 12.6 wt% but require heating above 300 °C for desorption e.g. LiH.[9,12] The volumetric energy density of metal hydrides is usually higher than for liquid hydrogen. The slow kinetics and high energy required for desorption makes metal hydrides infeasible for on-board hydrogen storage in light duty vehicles. [14, 20, 21] Complex hydrides have large storage capacities and require lower temperatures for desorption compared to metal hydrides, but have poor reversibility. [9]

Currently physisorption is the most promising storage technique due to its high storage density, reversibility and rapid sorption kinetics. The physisorption mechanism suggests adsorption of molecular hydrogen on the surface via relatively weak van der Waals bonding. Physisorption depends on two major factors, the specific surface area of the material and the temperature. [9, 14] The adsorption of hydrogen molecules is directly proportional to specific surface area of the adsorbent and inversely proportional to temperature. [15, 22] Further, an increase in adsorption is observed with an increase in pressure. [22] Several materials have been studied including carbon-based materials such as activated carbon and graphene as well as

other nanostructured materials including metal organic frameworks (MOFs) and covalent organic frameworks (COFs) [22, 23, 24, 25, 26]

1.2 Hydrogen storage systems

In addition to high storage capacities, physisorption offers advantages like on-board reversibility and rapid sorption kinetics. The major challenge for physisorption is the need to operate at very low *temperature* (below −150 °C) called cryogenic temperatures. Adsorption of hydrogen is an exothermic process. During adsorption, the heat of adsorption increases the bed temperature reducing the hydrogen storage capacity of the bed. Hence, it is necessary to remove the heat of adsorption to maintain the cryogenic temperature of the bed in order to maximize the storage of hydrogen. Complicating matters, the thermal conductivity of most adsorptive materials is low which increases the time needed for heat removal.

The use of heat exchangers within hydrogen storage vessels to manage the temperature of the storage bed has gained increasing attention in recent years. The majority of heat exchanger studies have been focused on metal hydride systems. A variety of heat exchanger designs have been proposed including external cooling of the storage pressure vessel with a coolant jacket [27], tube-fin heat exchangers with circular fins [28,34], plate-fin heat exchangers with different fin geometries [28,30,31,36], spiral or helical-tube heat exchangers with and without fins [27,32,33] and heat exchangers using aluminum foam [28,35]. Visaria et al. reported a fin and tube type heat exchanger which displaced 29% of the tank volume. [36] A coiled tube heat exchanger was reported which displaced 7% of the tank volume. [33]

2. Hydrogen Storage Thermal Management System Design

Microchannel process technology (MPT) has the potential to help achieve the long term goals of the DOE for light duty vehicle applications. Microchannel heat transfer devices use smaller fluid channels compared to traditional heat exchangers. Smaller fluid channels lead to shorter diffusional distances for heat transfer which increases the overall heat transfer coefficient leading to reduced size and weight of heat exchanger components by 2 to 10 times compared to traditional heat exchangers. [37,42]

Microchannel heat exchangers have not been widely studied for hydrogen storage applications. Muduwar et al reported the use of a microchannel heat exchanger for a metal hydride hydrogen storage but no details are available regarding heat exchanger performance in light of DOE targets [38]. Steigleder reported the design and testing of a thermal management system (TMS) for adsorption based hydrogen storage. The current study builds on these previous findings to demonstrate a cooling strategy for adsorption systems capable of improving the size and weight over the state-of-the-art TMS. [41]

2.1 Modular Adsorption Tank Insert

Figure 1 shows the concept for a unit cell within a microchannel-based thermal management system (TMS) for managing the temperature within a hydrogen storage adsorbent bed. In the concept, an adsorbent bed (activated carbon) 30 cm in diameter and 2.5 cm in height is used to store hydrogen at liquid nitrogen temperatures and 50

atm of pressure. Hydrogen within the tank is prevented from adsorbing radially using a diffusion barrier but instead is distributed radially through a hydrogen distribution plate and is adsorbed axially within the bed providing a more uniform heat load on a microchannel cooling plate. The heat of adsorption is removed 1) through the distribution of the chilled hydrogen (typically transported at 27 K) in the hydrogen distribution plate; and 2) using liquid nitrogen (LN2) entering the cooling plate at 70 K.

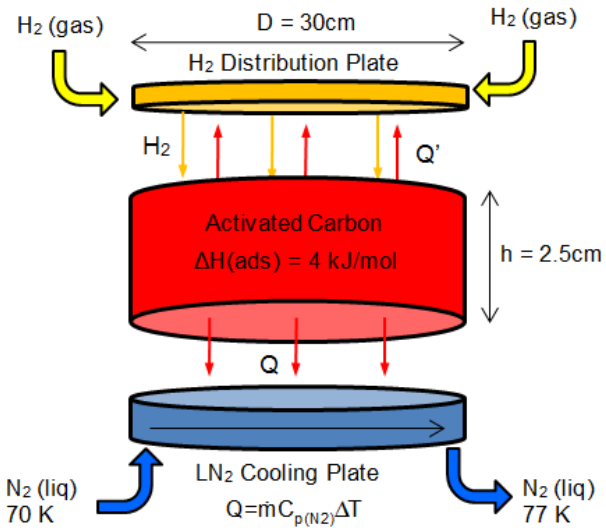

Figure 1: Basic concept of function of Thermal Management System

To manage the temperature within a full-scale adsorption bed, multiple adsorption modules are needed. Figure 2 shows the cross-section of a Modular Adsorption Tank Insert (MATI) consisting of four 30 cm diameter modular adsorption beds interleaved at 2.5 cm intervals with an alternating set of liquid nitrogen cooling (LN_2) and hydrogen distribution plates (H_2). Distribution of LN2 to the cooling plates is managed using tubular headers. Requirements for the MATI are to store 5.6 kg of

hydrogen within a fill time of 3 minutes. During H2 fill, the bed is cooled by the incoming stream of chilled H2 which is supplemented with LN2 cooling.

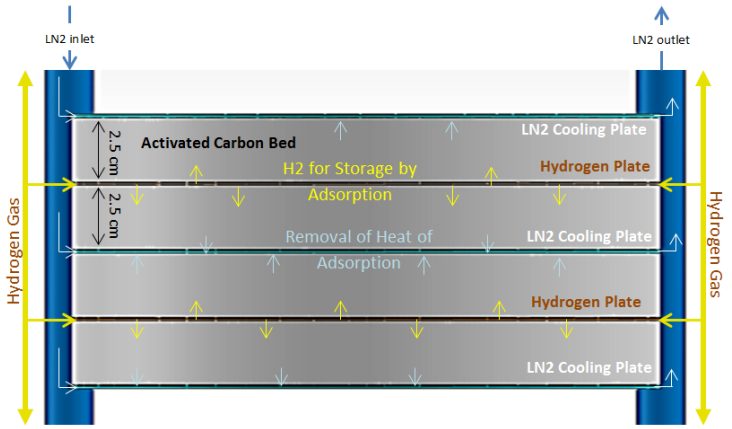

Figure 2: Schematic of Modular Adsorption Tank Insert showing the basic functionality of the system

The number of cooling plates and distribution plates required depends upon the module height. The module height is the most critical feature in the design. In order to maintain reasonable storage efficiencies, the temperature of the bed should be maintained at cryogenic temperatures (at or below 77 K at atmospheric pressure or 83.5 K at 2 bar gage pressure). If the module height is too small, the number of cooling plates required increases, increasing the size and weight of the system. If the module height is too big, the hydrogen storage efficiency decreases due to an increase in the bed temperature.

In previous work, Steigleder [41] successfully demonstrated a sub-scale stainless steel MATI showing the ability to remove heat at a rate consistent with the heat of adsorption from adsorption uptake during hydrogen fill. The reported displacement volume of the MATI obtained was 160.9 L which for 316 SS leads to a mass of 136.4 kg. It was recognized that one strategy to reduce the weight of the MATI would involve the use of aluminum alloys.

Further, Steigleder [41] developed a series of process-driven cost-of-good-sold models and reported that the major cost drivers in MATI manufacturing was the high raw material cost and consumable costs associated with the photochemical machining (PCM) of stainless steel. The third cost driver was found to be the yield of the diffusion bonding process. Cost models were developed by Steigleder to evaluate the effect of changing from the PCM and diffusion bonding of stainless steel to the PCM and laser welding of aluminum alloys on the cost of the MATI. These changes in material and process strategy for the MATI were expected to provide a cost reduction of approximately 24%. The use of laser welding in concert with stamping was found to provide acceptable costs based on input from HSECOE team members. Details of the stainless steel and aluminum cost models can be found in [41].

The aluminum alloy used in the cost model study was 3003-O aluminum alloy. Considering the above process plan, the material shows good properties for stamping but poor joint strength after laser welding [43]. Due to this reason 6061-T6 aluminum was chosen based on good ductility and weldability. Since it is a heat treatable alloy, the reduction in the weld joint strength can be remedied by post weld heat treatment.

The use of aluminum alloys actually increases the size of the TMS due to the lower strength-to-volume ratio for aluminum alloys compared to stainless steel. As an example, based on plate mechanics, 6061-T6 would require a plate thickness about 1.4 times that of 316 stainless steel to achieve the same deflection for a given span. At the same time, the density of the aluminum alloy is about 2.9 times lighter. Consequently, the mass of the 6061-T6 beam would be about 2.1 times lighter

compared with stainless steel. However, the problem with adsorption beds is volumetric density not gravimetric density. This problem was addressed (below) by enhancing the conductivity of the adsorbent bed leading to larger bed heights and the need for fewer cooling plates.

2.2 Aluminum MATI TMS Design

The function of the liquid nitrogen cooling plates are to remove the heat of adsorption during hydrogen filling and to provide heat for desorption during the operation of the vehicle. The flow rate requirements during adsorption are much greater than those needed for desorption, hence the system was designed primarily for the adsorption event. Material requirements included the need to resist hydrogen permeation and embrittlement at cryogenic temperatures and 50 bars of pressure as well as to resist erosion due to the potential for high LN2 velocities and be joinable for hermeticity. In addition to this, the LN2 cooling plate needed to withstand hydrogen pressures of at least 50 atm at cryogenic temperature without significant fin deflection which can lead to higher pressure drops or flow maldistribution across the plate. Poor flow maldistribution could cause hot spots within the adsorbent bed reducing the hydrogen storage capacity of the bed.

2.2.1 Detail Design

Models of the Al MATI design were developed in Solidworks. The top plate is 30 cm in diameter with a 0.25 mm thickness containing inlet and outlet holes of 15

mm in diameter for liquid nitrogen headers. Figure 3 shows the top view of the LN2 top plate.

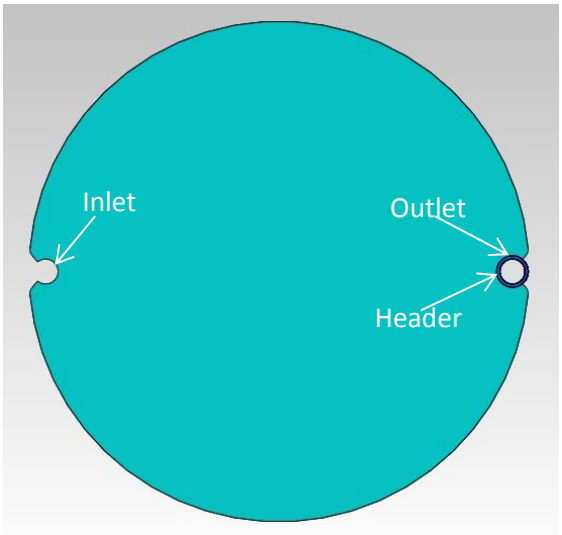

Figure 3: Top view of liquid nitrogen top plate

The 30 cm diameter bottom plate is a 0.5 mm thick plate with similar holes for inlet and outlet headers. The plate is photochemically machined down to a thickness of 0.25 mm in channel areas with circular pillars of 0.7 mm diameter evenly distributed throughout the plate providing a span of 3.25 mm as shown in Figure 4. These pillars minimize deflection of the microchannel fins during filling. The bottom plate contains a 1.5 mm thick rim at the circumference of the plate to provide a weld boss for laser welding. A circular ring of nearly rectangular pillars, 0.7mm wide, provide a means to evenly distribute the liquid nitrogen entering the plate. Circular weld bosses of 2 mm in diameter are distributed throughout for spot welding the bottom plate to the top plate.

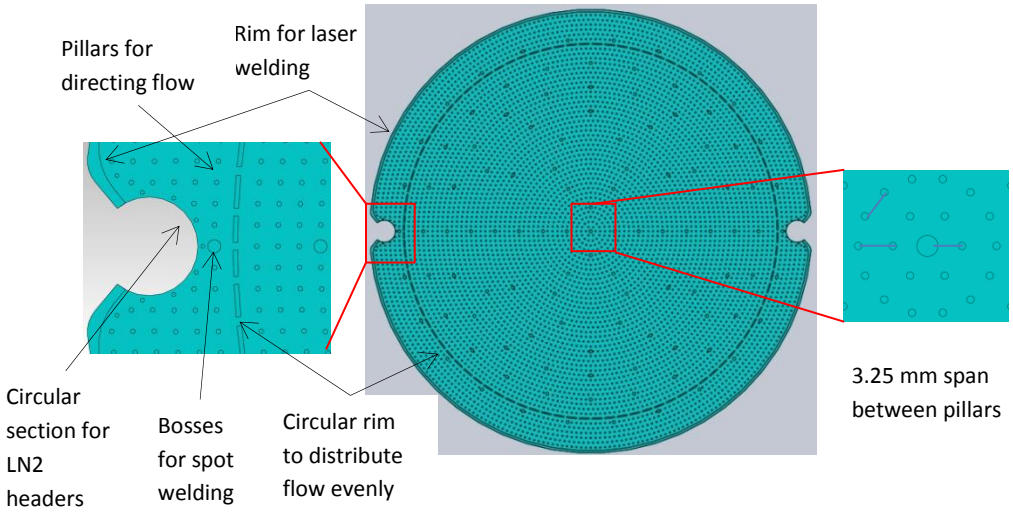

Figure 4: Top view of liquid nitrogen bottom plate showing inlet, rim for welding, spot welding bosses, circular and rectangular pillars and flow distribution and span between pillars.

To help with material selection, a mechanical analysis was performed on the design using Abaqus finite element analysis (FEA) software. Based on plate mechanics, the span between pillars was chosen to keep microfin deflection below 5% of the channel height based on 0.7 mm diameter pillars and an isotropic differential pressure of 50 atm on the outside of the welded cooling plate. This threshold was chosen based on the work of Paul and Wattanutchariya [42] who concluded that microchannel size variations of less than 5% across a microchannel array have minimal impact on flow maldistribution and heat exchanger performance. FEA analysis was performed on the plates at different locations to evaluate the local deflection of the microchannel fin. It was found during the analysis that the properties of heat exchanger aluminum (3000 series) were insufficient to minimize deflection. Consequently, it was determined that a 6000 series heat-treatable aluminum alloy would be required. The properties of the material used in the analysis were a Young's modulus of 68.5 GPa and a yield strength of 276 MPa based

on the properties of 6061-T6 aluminum. A span between pillars of 3.25 mm was found to be suitable. The radius of the pillars is equal throughout the cooling plate. The minimum distance between the adjacent pillars is 3.25 mm and evenly spaced along the circumference of that radius. Hence the span between the two pillars varies with a minimum and maximum span of 3.25 mm and 5.63 mm, respectively. The FEA analysis was performed based on the maximum span obtained in order to eliminate deflection of the fin. The maximum deflection obtained in the channel was found to be less than 4% of the channel height. Figure 5 shows the FEA results and the location that the analyses were performed.

Based on the Fluent computational fluid dynamic (CFD) analysis of the flow and thermal distribution of the device in prior work [41], estimates were made for the pressure drop of the 30 cm diameter plate. The design features in the stainless steel design and the current aluminum design were similar except the circular rim width along the circumference, diameter of the pillars and span between pillars. Based on Poiseuille flow assumptions, the pressure drop was estimated to increase by a small amount. This was due in part to a higher flow rate required to remove the heat of adsorption due to a decrease in the hydraulic diameter caused by an increase pillar diameter (photochemical machining constraints). It was expected that the flow distribution would not differ significantly between the designs.

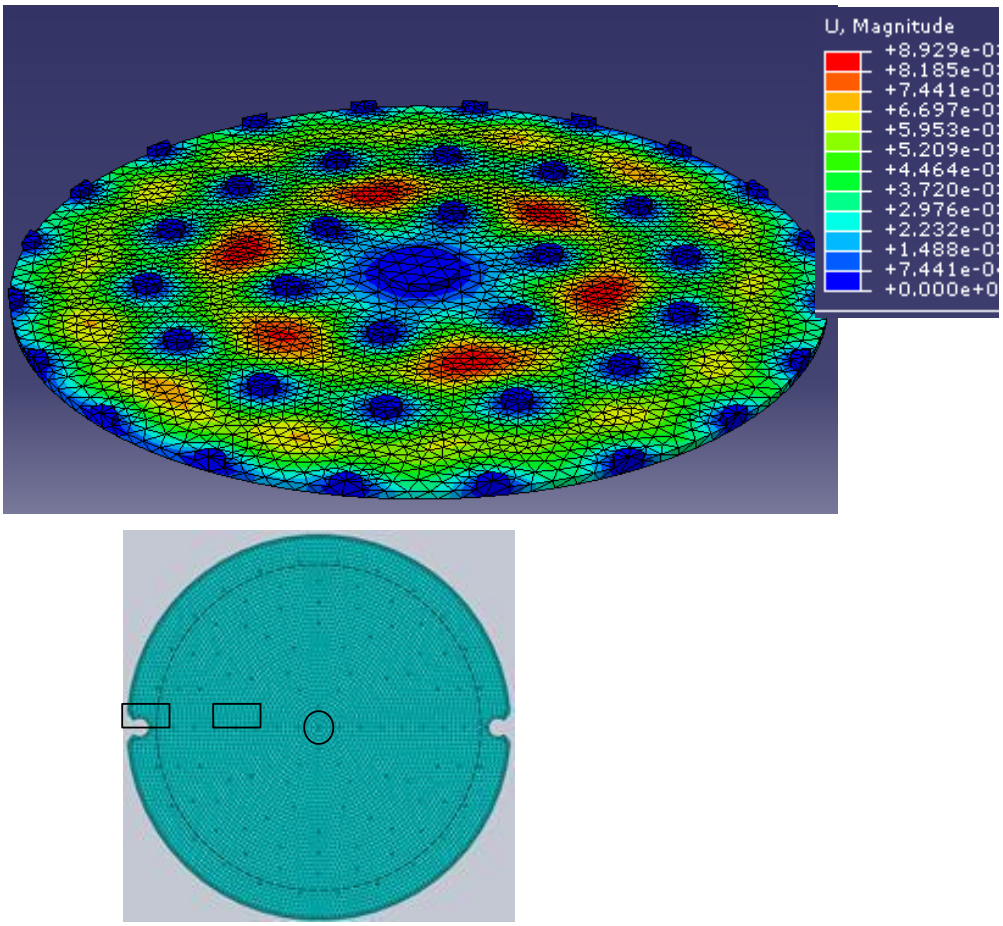

Figure 5: (Top) FEA analysis results at the center of the liquid nitrogen cooling plate. (Bottom) Cooling plate design showing locations where FEA was performed. Largest span was found to be at the center of the cooling plate.

For the overall MATI system, a header was designed with a 15 mm inner diameter and a 2 mm wall thickness having slots every 50.6 mm for connection to the inlet and outlet of the LN2 plate. Figure 6 shows a rendering of the liquid nitrogen header.

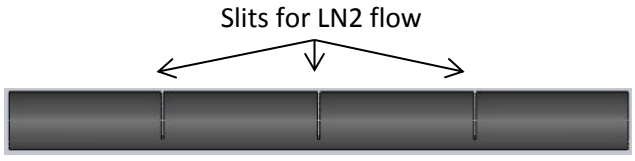

Figure 6: Rendering of the liquid nitrogen header.

The hydrogen distribution plate consisted of a top plate and a bottom plate. The top plate is 30 cm in diameter with a 0.25 mm thickness having holes for the LN2 headers. The plate contains an array of 0.35 mm diameter holes over the area of the plate to provide axial access for the hydrogen gas to the adsorbent bed. Figure 7 shows the top view of the hydrogen distributor top plate.

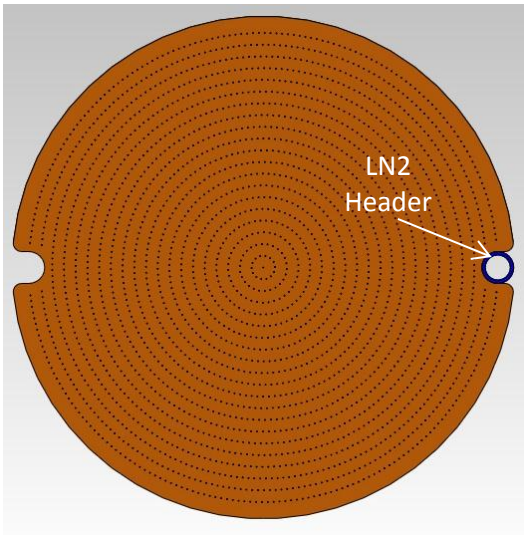

Figure 7: Top view of hydrogen distributor top plate

The H2 bottom plate is 0.35 mm thick with a 0.1 mm deep channel height. Like the LN2 cooling plate, the microchannel contains a host of 0.7 mm diameter pillars throughout the channel to resist fin deflection. The rim of the device provides a 1.5 mm wide welding boss which is relieved 0.1 mm in thickness periodically to provide radial access into the adsorption bed for the hydrogen. Figure 8 shows the top view of hydrogen distributor bottom plate with the detailed features. The circular rim is welded except at the reliefs. Every other line pillar contains slits and through holes of 0.35 mm to provide axial access for the hydrogen to the adsorbent bed. Bosses of 2 mm in diameter are provided for spot welding of the plates.

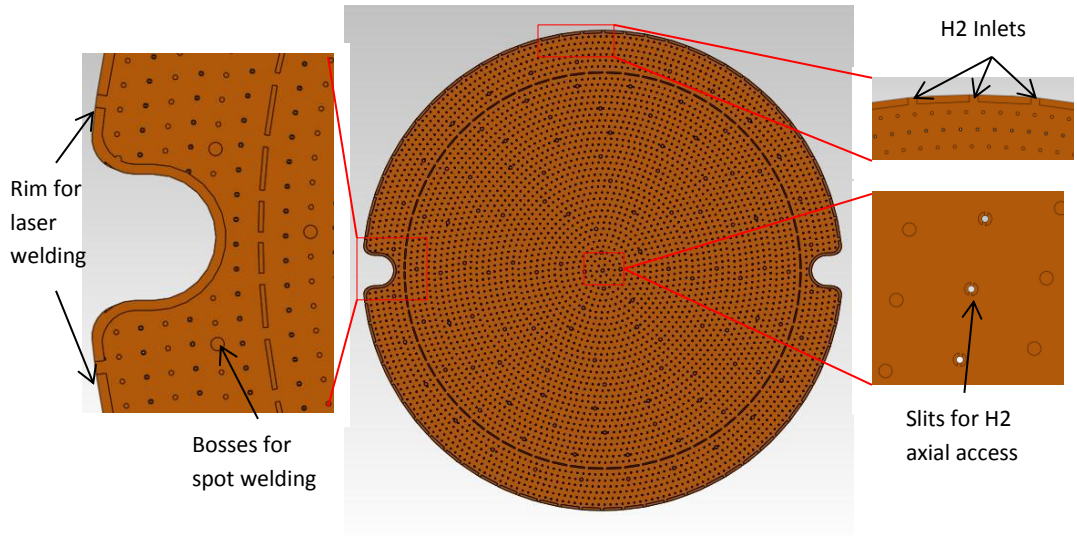

Figure 8: Schematic of hydrogen distributor bottom plate showing the rim for welding, spot welding bosses and slits for hydrogen axial access and hydrogen inlets.

Based on the above design, the system mass and volume were calculated for the complete system. Table 2 shows results for the mass and volume of the system with and without the adsorbent bed. The thermal management system (TMS) occupies approximately 5.0% of the internal tank volume and the TMS mass is about the 10.3% of the overall mass of the MATI system. This is an 83% reduction in volume compared to prior fin and tube arrangements [36] and a 28% reduction compared to prior helical tube configurations [33]. Further, the volume of the system is reduced by 28% compared to the previous microchannel configuration designed by Steigleder. [41] This decrease is primarily due to an increase in the height of the adsorbent bed based on thermal conductivity enhancement of the adsorption bed (see above). As expected, the overall mass of the proposed Al TMS system is expected to decrease by 80% over the stainless steel TMS developed by Steigleder. [41]

Table 1: Expected mass and volume of the Al MATI TMS.

Volume of System			
TMS Displacement Volume	7.30 L	**5.04%**	Including extra 0.05m space at the top for header connections
MATI System Displacement Volume	145.14 L	100%	Minimum displacement volume required
Mass of System			
TMS Mass	8.81 kg	**10.32%**	LN2 and H2 plates and header mass
MATI System Mass	85.39 kg	100%	TMS, adsorbent bed and stored hydrogen mass

2.2.2 System Design

An overall system design was developed to evaluate the size and weight of the MATI based on the number of cooling plates required and LN2 flow rate required to meet the performance objectives of the system. The properties of activated carbon, hydrogen and liquid nitrogen used in the current study are shown in Table 1 below.

Table 2 : Properties of adsorbent, hydrogen and nitrogen for analysis

Adsorbent Density	520	kg/m^3	Heat of Adsorption	4000	J/mol
Hydrogen Storage Capacity	0.0799	kg H2/kg adsorbent	Liquid Nitrogen Heat Capacity [C_p]	2402	J/kg-K
Hydrogen Atomic Weight	0.0010	kg/mol	Liquid Nitrogen Density [ρ]	808	kg/m^3

The total length of the 30 cm diameter adsorbent bed required to store 5.6 kg of hydrogen was found to be 1.91 m. The average heat flux generated during the three minute fill time was found to be 62.5 kW. In order to remove this amount of heat

flux (Q), the required mass flow rate of the LN2 was determined using the following equation:

$$Q = \dot{m}C_p\Delta T \quad \text{(Equation 1)}$$

where $\dot{m}$ is the mass flow rate [kg/s] of LN_2 (liquid nitrogen), Cp is the specific heat capacity [J/kg-K] of LN_2 and ΔT is the change in temperature [K] of LN_2.

Assuming a maximum allowable bed temperature is 80 K, it was further assumed that the hydrogen gas provides some cooling capacity in entering the tank at 40 K. Assuming an average temperature difference of 30 K and a specific heat capacity of the hydrogen gas as 13,758.62 J/kg.K, the amount of heat removed by the hydrogen gas is about 12.8 kW. Thus the remaining amount of heat required to be removed by the liquid nitrogen is 49.7 kW.

Assuming that the liquid nitrogen is delivered at 70 K, the average temperature difference of the liquid nitrogen is expected to be 7 K to prevent boiling (assuming atmospheric conditions). Therefore, the liquid nitrogen flow rate required to remove the remaining heat of adsorption is 219.3 L/min when hydrogen cooling is taken into consideration. This requires subcooling of the liquid nitrogen to 70 K before entering the inlet of the tank. Alternatively, the boiling temperature of the LN2 can be increased by increasing the pressure of the liquid nitrogen at the inlet of the tank.

As mentioned above, the volumetric density of an Al MATI TMS was a concern. One means to address this was to reduce the number of cooling plates required by increasing the conductivity of the adsorption bed. Efforts were made by the HSECOE team to increase the module height based on strategies for inserting Al pins within the modular beds to reduce transport distances. Based upon analyses

performed by Truszkowska et al. [39,40] it was found that a module height of 5 cm could yield reasonable hydrogen storage efficiencies through thermal conductivity enhancement of the bed.

A module height of 5 cm results in the need for 39 modules with each adsorption bed containing one hydrogen distribution plate embedded on the center plane of the module and cooling plates on either side of the module. Consequently, 39 hydrogen distribution plates and 40 LN2 cooling plates are required to successfully remove the heat of adsorption from an activated carbon bed 1.91 m in length and 30 cm in diameter necessary to store 5.6 kg hydrogen in 180 seconds. Thus, the cooling capacity requirement per cooling plate is to remove 1,273.7 W per cooling plate (equals 636.8 W per side of cooling plate) requiring a liquid nitrogen flow of 219.39L/min. In order to evaluate the size and weight of this system, a detail design was developed in order to evaluate the weight and volume of the aluminum MATI.

3. Manufacturing Process Plan for the Al MATI TMS

A manufacturing process plan was developed for the MATI TMS in order to develop a cost model. The cooling plates were designed to be photochemically machined to form flow channels. The hydrogen plates are punched to form holes for axial access for the hydrogen to the adsorbent bed. Both the hydrogen and liquid nitrogen plates are then joined together using laser welding. Headers of 6061-O aluminum alloy are cut to desired length and the slots are machined into the headers for assembly with the cooling plates. Machining the material in annealed condition and then heat treating the material provides several advantages for cost reduction including reduced cycle times and machining forces while providing higher post-heat treatment yield strengths. Vacuum brazing is used to join the header to the cooling plates.

The assembled TMS must be heat treated to increase the strength of the material after assembly. This heat treatment would be needed after vacuum brazing due to exposure to thermal cycles during brazing.

Precipitation-hardening heat treatment consists of solution heat treatment at 565 ˚C for 40 minutes in an inert atmosphere and quenching in a medium such as water, oil or in air by free convection. It is followed by artificial aging at 160 ˚C for 18 hours.

The manufacturing plan is shown in the figure 9 below.

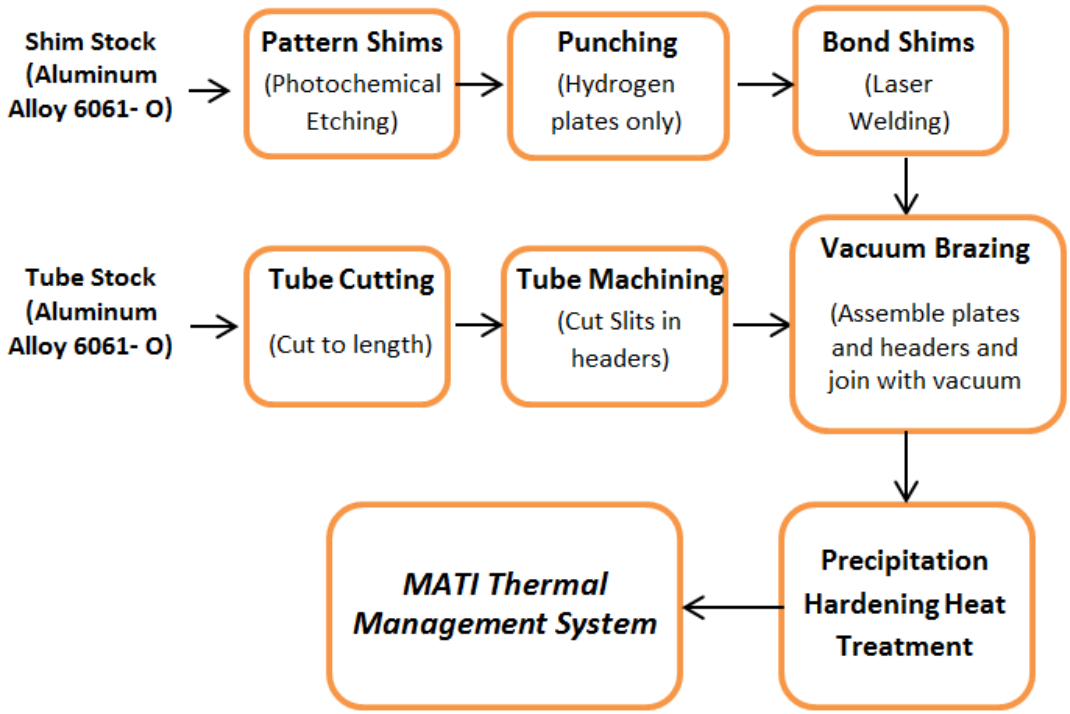

Figure 9: Manufacturing plan for MATI

The use of laser welding in concert with stamping was found to provide acceptable costs based on input from HSECOE team members. Details of the cost model results are reported in [41].

3.1 Manufacturing with Aluminum Alloys

Precipitation-hardened aluminum alloys are very popular in the industrial world due to their high strength to weight ratio, light-weight, good ductility at subzero temperatures, high resistance to corrosion, and non-toxicity. One challenge with aluminum alloys is that they are notoriously difficult to join because of the tenacious native oxides on the surface of the metal. Surface oxides make diffusion bonding

difficult and can result in oxide inclusions during fusion welding. Further, the high thermal conductivity of aluminum makes thermal accumulation, phase change and coalescence of surfaces more difficult leading to larger heat-affected zones. To overcome these issues, laser welding was chosen because of the high energy densities available leading to smaller heat affected zones. Another challenge with the fabrication of micro-scale geometries using precipitation-hardened aluminum is warpage as a result of heat treatment. In particular, quenching after solution heat treatment can cause significant thermal gradients that can plastically strain the material.

3.2 Joining of Aluminum Alloys

Different bonding and diffusion brazing techniques have been reported for the joining of aluminum alloys. The major disadvantage with diffusion bonding is the high temperature required for bonding. Diffusion bonding is normally carried out at about 50-70 % of the absolute melting point of the parent material. Aluminum alloys are prone to oxidation at high temperatures and hence high pressure is required to crack the oxide layer and join the faying surfaces. Besides this, the requirement of inert atmosphere or vacuum and long bonding cycles makes diffusion bonding and diffusion brazing expensive methods for joining.[46, 47]

Conventional welding methods available for joining aluminum include shielded metal arc welding, gas-tungsten arc welding, plasma arc welding, gas- metal arc welding, electron beam welding and resistance spot welding among others [48]. The disadvantages associated with conventional welding, are the low aspect ratios

compared to electron and laser beam welding, the large heat affected zone, high distortion and slower welding speeds.

Laser welding offers several advantages over conventional welding methods including short cycle times, high weld quality, high weld aspect ratio, low heat input, low distortion, manufacturing flexibility and ease of automation [49]. The two fundamental modes of laser welding are: a) conduction welding and b) keyhole or penetration welding. The two modes of welding are illustrated in Figure 10.

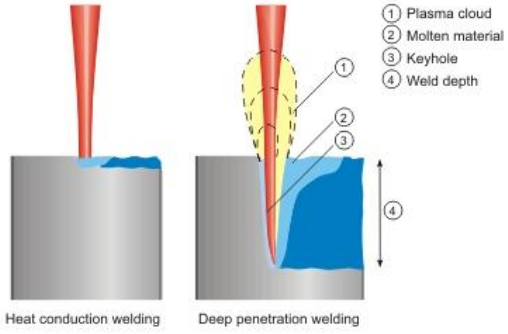

Figure 10: Modes of laser welding (a) Conduction welding, (b) Keyhole welding

In conduction welding, the surface of the material is heated above its melting point but below its vaporization temperature. Fusion occurs only by heat conduction through the welding melt pool, the weld pool has strong stirring forces driven by Marangoni-type forces resulting from variation in surface tension with temperature. Most conduction limited welds are employed with an out-of-focus beam. The weld depth to width ratios of 1:2 or less are obtained with conduction welding, hence conduction welding is limited to thin materials. Since the laser radiation does not penetrate into the material they are less susceptible to gas or oxide entrapment during welding. [49, 51]

In keyhole welding, there is sufficient energy per unit length to cause local vaporization to form a keyhole. This hole is stabilized by the pressure from the vapor being generated. The keyhole behaves like an optical black body in that the radiation enters the hole and is subject to multiple reflections before being able to escape. The absorptivity of the material at the start of the keyhole jumps up from 3% for highly reflective materials to 98% once the keyhole is initiated. [49, 51] With keyhole welding, intermittent closure of the keyhole can result in porosity [52]. Keyhole laser welding results in better energy coupling, higher weld depth and high speed necessary for economic considerations, hence most of the laser welding applications are centered about the deep penetration welding. [49]

During laser keyhole welding there are three different regions that are produced, the fusion zone (FZ), the partially melted zone (PMZ), and the heat affected zone (HAZ). These regions have been categorized based on the temperatures that occur during welding. The thickness of these three zones put together is usually much narrower than conventional welding techniques [50].

The material in the fusion zone is completely melted during welding with temperatures surpassing the liquidus temperature of the alloy. According to a study performed on laser welding alloy A6061-T6 [53] with a CO2 laser, the FZ was found to be approximately half the width of what it was in TIG welded joints. The defects found in this region are usually porosity, solidification cracking and sometimes loss of alloying elements [50]. The solidification rates of 105 to 106 oC/sec are obtained due to high energy density laser resulting in low heat input at high travel speeds. Thus the fusion zone of laser weld is characterized by fine-grained microstructures. The

grain structure in laser-welded 5000 and 6000 alloys primarily consists of fine columnar dendrites originating from the fusion line and some equiaxed grains in the weld center. [47, 54] The amount of equiaxed grains decreases with increasing travel speed [55, 56]

The PMZ experiences temperatures between eutectic and liquidus temperatures of the alloy. Liquation cracking may occur along the weakened grain boundaries in the PMZ. The PMZ in laser welded aluminum alloys is generally narrow approximately one or two grains wide. [50, 57]

The HAZ is the outermost area of the three and the maximum temperature experienced is below eutectic temperature of the alloy and hence no melting occurs in this zone during welding. The hardness of the HAZ zone falls below 90% of the base metal and hence is called the softened region. It has been shown that the widths of softened regions in the HAZs of the laser welds are of the order of one seventh to one quarter those for TIG welds [53]. In non-heat-treatable aluminum alloys, softening occurs because of localized annealing in HAZ by grain growth or loss of strain hardened structure. However, in heat-treatable alloys, welding heat will destroy the temper in the HAZ. Softening in precipitate-hardenable alloys involves the dissolution of strengthening phases and formation and growth of non-strengthening phases [58]. Heat treatable alloys are also susceptible to liquation cracking in the HAZ. [50]

Aluminum alloys have high reflectivity and thermal diffusivity requiring the high absorptivity available via laser keyhole welding. Laser keyhole welding will provide

large penetration depth with relatively low energy input leading to smaller HAZs and less material warpage.

3.3 Laser Welding

Weld depth is an important welding attribute since weld depth dictates the thickness of the material that can be welded. Weld depth is influenced by the wavelength of the laser, beam diameter at focus, laser power, scan speed and more importantly the properties of the material.

3.3.1 Defect Modes

Several researchers have sought to understand the laser welding of aluminum alloys including potential defect modes and the effects of these defects on the properties of the weldment. The major defects present in the aluminum weld joint are reported below.

Laser welded joints have the potential for a variety of defects. The deep keyhole can be made unstable based on energy input and welding time leading to several defects in the weld joint. There are four major categories of defects: a) porosity, b) cracking, c) inclusions and d) loss of alloying elements. [50]

3.3.1.1 Porosity

Hydrogen porosity: Laser welding is very susceptible to hydrogen porosity since hydrogen is very soluble in aluminum and its alloys. Most gas porosities precipitated

in aluminum alloys are attributed to hydrogen. The solubility of hydrogen in liquid aluminum is an exponential function of temperature and hence it becomes a huge problem in laser welding compared to conventional welding. The cooling rate of the melt pool being high for laser welding it does not allow diffusion or floatation of the trapped hydrogen. Different alloys of hydrogen have different level of affinity towards hydrogen solubility, thus the threshold level of hydrogen for the formation of hydrogen bubbles is different for different materials. [50, 59]

Hydrogen in molten aluminum is mainly formed by the reaction of molten aluminum and water vapor. The hydrogen may originate from the base metal itself, oxides or hydroxides, or other materials on the contaminant surface, or welding atmosphere or shielding gas. The normal levels of hydrogen content in aluminum vary between 0.10 to 0.04 mL/100g. [50] The tolerable hydrogen content in the welded joint has not been reported so far.

Possible measure to reduce the hydrogen porosity needs to be taken by reducing the hydrogen sources before and during welding. The welding surface should be free of all contaminants and oxides and high-grade shielding gas should be used. [58] Higher power density at the workpiece keeps the keyhole stable during welding and increases the solidification time, thus allowing hydrogen to escape from the weld pool. It has been reported that higher power continuous wave Nd:YAG laser welding causes a reduction in gas porosity. [61]

Porosity caused by the collapse of unstable keyholes: The vaporization in the keyhole is not uniform and their position vary with time, thus the keyhole fluctuates vary rapidly. [34] Keyhole stability during laser welding depends to a high degree on

the balance of forces active inside the keyhole. Upon establishment of the vapor cavity, the fluid forces of the molten pool are balanced by the vaporization pressure within the cavity. The inherent instability of the keyholes may lead to periodic collapse of the liquid metal surrounding the vapor cavity causing the formation of periodic voids [35].

Another probable reason of porosity formation in the weld joint is due to entrapment of gases into the liquid metal due to turbulent flow in the weld pool and porosity due to shrinkage during solidification. [50]

The way to reduce this porosity is to keep the keyhole stable by using high welding speeds [60] Use of high power density at the workpiece and suitably adjusting the defocus of the laser beam has been reported to maintain the keyhole stable [50,62]

3.3.1.2 Hot Cracking

Aluminum alloys exhibit a strong propensity for welding crack formation because of their large solidification temperature range, high coefficient of thermal expansion, and large solidification shrinkage. The two main types of cracks are liquefaction cracking in heat affected zone and solidification cracking in fusion zone of laser welded aluminum alloys. [57]

HAZ liquation cracking: Fine cracks may be formed at the low melting point grain boundary films in HAZ due to thermal stresses induced during welding. [63] Liquation cracking usually takes place in heat-treatable alloys as a result of the large quantities of alloying additions that are available to form eutectic phases with low

melting points. Liquation cracking can be reduced by minimizing heat input and small HAZ and PMZ. [50]

Solidification cracking: Solidification cracking occurs at high temperatures above the solidus under circumstances where the material has low ductility and is under high contraction stresses. Solidification of the liquid weld metal begins at one temperature (the liquidus) and completes at a somewhat lower temperature (the solidus). Between the two levels the alloy forms an incompletely solidified mass which is brittle and has little or no ductility until cooled to lower temperatures. The brittleness is present in liquid films which surround the solidifying grains or dendrites and when subjected to the high transverse contraction stresses, during weld cooling, solidification cracking may result in the film boundaries; usually those near the centerline of the weld which are the last to cool. [50, 67]

3.3.1.3 Oxide Inclusions

Oxides are one of the main types of inclusions in aluminum alloys. During keyhole laser welding the unstable keyhole flow may entrap shielding gas or even air because of imperfect gas shielding [58]. Thus, some oxides particles may occur in the keyhole forming oxides films due to impurities present in the gas.

When aluminum alloys contain magnesium, because it is surface active in liquid aluminum, the oxidizing tendency of the molten aluminum increases rapidly with magnesium contents. Depending on the Mg content in the aluminum alloy, different Mg oxides are formed, when the magnesium content of the alloy exceeds approximately 2%, the liquid oxidizes rapidly to form MgO. [50]

3.3.1.4 Loss of alloying elements

The high power density used for laser welding may cause selective vaporization of some alloying elements with low fusion point such as lithium, magnesium, and zinc because of their higher equilibrium vapor pressure than aluminum. Selective vaporization of alloying elements can take place in both keyhole and conduction mode laser welding. The vaporization mechanism is divided into three stages. The first involves transport of vaporization elements from the bulk to the surface of the molten weld pool. Then the vaporization of elements occurs at the liquid/vapor interface, and finally the vaporized species are transported into the surrounding gas phases [50]. This will also cause a void on the top of the weld called underfill. It was found that the intrinsic vaporization of alloying elements at the weld pool surface controls the overall vaporization [57].

The loss of alloying elements can be minimized by controlling the beam power density distribution during continuous wave (CW) laser welding, which can influence the temperature of the molten metal in the welding pool [50]. Another way of reducing this loss is through the use of filler metal, which is used as an auxiliary source of material to fill the gap.

3.3.2 Strategies for Aluminum Laser Welding

The techniques available to minimize defect formation in aluminum laser welding include varying scanning speeds and laser power as well as the use of shielding gases and filler metals. Use of one technique would reduce one type of defect but cause another type of defect e.g. porosity can be reduced by using high power density at

high welding speed but it can lead to liquefaction cracking of the weld joint. Therefore, one need is to find the right combination of techniques that would produce the highest weld strength with hermeticity.

Batahgy and Kutsuna reported 5 kW CO2 butt welding of 5000 and 6000 series and 2 mm thick alloys and investigated the several defects at different process parameters.[64] Hirose et al. reported butt welding of 6061-T6 aluminum alloys using 2.5 kW CO2 laser at 167 mm/s speed. The weld strength and hardness in 3 zones was compared to TIG welding. [53] Kawamoto et al reported lap joint welding of 1mm thick 6061-T6 aluminum alloy using YAG laser and filler metal. The effect of gap between the two plates on the strength of the weld joint was investigated. [65] Ramasamy et al reported that when welding with a pulsed 2 kW Nd:YAG, or a 3 kW continuous wave Nd:YAG, or a 3-5 kW CO2 laser, vaporization of magnesium and/or silicon can occur from aluminum alloy 6111-T4 and also the metal hardness was reduced. Thus, when welding at high power densities loss of alloying elements is a significant problem. [66]

Dausinger, et al. reported that with a 2.2 kW Nd:YAG laser, weld depths of up to 3.7 mm in AA 6082 have been obtained at approximately 16.7 mm/s, at a power density of 3 MW/cm2.[67] A 4.5 kW CO2 produced weld depth of 3.5 mm in 5000 and 6000 aluminum alloy series at a speed of approximately 33 mm/s. In comparison, a 4 kW Nd:YAG produced weld depths of 4 mm at same speed [50] A 3 kW CO2 laser has been able to achieve approximately 2.5mm weld depth in aluminum alloy 7075-T6 at about 25 mm/s[68]. In comparison, Paleocrassas et al reported 300 W

ytterbium fiber laser welding of 7075-T6 achieving weld depth of 1mm at 2mm/sec showing higher joining efficiency compared to CO2 laser. [69]

3.3.3 Warpage in microchannel arrays

Warpage refers to any distortion from the intended shape and design of an object or material. This usually results from an uneven distribution of plastic stress and is most often caused by thermal gradients during manufacturing. Warpage can also be caused by the relaxation of uneven residual stresses within a material. Because of the small feature sizes within microchannel arrays, warpage is a concern. Uneven warpage of fins across an array can lead to flow maldistribution which in turn significantly reduces the efficiency of the device.

In the current study the microchannel device is manufactured using a 6061-O aluminum alloy which is more susceptible to warpage than stainless steels and nickel superalloys which have better mechanical properties. Further, the proposed manufacturing process consists of PCM, laser welding and precipitation hardening heat treatment to increase the strength of the material to 6061-T6 condition. Warpage can be induced in any of these steps. For example, residual stresses embedded in both sides of the material during cold rolling can cause warpage after PCM due to the one-sided removal of material. To compensate, these stresses are typically relieved via thermal annealing prior to PCM to reduce the warpage.

3.3.3.1 Warpage due to laser welding

Another potential source of warpage are the thermal gradients generated during laser welding. During laser welding, the parts are locally heated by intense laser beam followed by melting and solidification. Distortion in a weld results from the expansion and contraction of the weld metal and adjacent base metal during the heating and cooling cycle of the welding process. During this heating and cooling cycle, many factors affect shrinkage of the metal and lead to distortion, such as physical and mechanical properties that change as heat is applied. For example, as the temperature of the weld area increases, tensile and yield strength, elasticity, and thermal conductivity of the aluminum decrease, while elongation, thermal expansion increase. These changes, in turn, affect heat flow and uniformity of heat distribution. [78]

Due to the non-uniform temperature distribution during the thermal cycle, incompatible strains lead to thermal stresses. These incompatible strains due to dimensional changes associated with solidification of the weld metal, metallurgical transformations and plastic deformation, are the main sources of residual stresses and distortion. [73]

FEA of residual stress and distortion in welding process have been studied by various researchers. An analytical model was proposed to examine the residual stress distribution across the weld of panels welded with mechanical constraints.[74], Furthermore, a novel measuring method of three-dimensional residual stresses based on the principle which is simplified by utilizing the characteristics of the distribution of inherent strains induced in a long welded joint was proposed [75]. Residual stress

and distortion in the weldment has been reported by several other authors' [73, 76]. Experimental evaluation of the residual stress in the weldment was performed by J. Costa et al [77]. No literature was found reporting the experimental evaluation and analysis of warpage and distortion due to laser welding in 6061 aluminum.

3.3.3.2 Warpage due to heat treatment:

For 6000 series aluminum, heat treatment is also a major source of warpage. Precipitation hardening of 6061 aluminum alloy consists of a solution heat treatment at temperatures close to the eutectic temperature of the alloy followed by rapid quenching. Afterward the material can be artificially aged at lower temperatures to a fully-hardened T6 condition. According to the ASTM standard for the heat treatment of wrought aluminum alloys (B918/B918M-09), solution heat treatment is generally carried out between 516-579 °C and kept at that temperature depending upon the maximum thickness of the material. Rapid quenching may be performed in water to obtain high cooling rates. Other options for quench media include glycol, oil, forced air and water spray among others.

The rapid quenching of the material induces high cooling rates. Thin microchannel laminae are particularly susceptible to even small thermal gradients in the material temperature lead to thermal stress-induced warpage of the material. [45] The literature reports the use of several quench media which reduce the cooling rate, and hence the warpage, in the material.

In summary, the laser welding of 6061 aluminum for producing hermetic joints in microchannel components has not been studied nor reported in the literature. Further, no studies have been reported regarding the hermeticity of laser weldments in 6061 aluminum. Potential sources of microchannel warpage include laser welding and heat treatment. These investigations are necessary to apply laser welding to heat-treatable aluminum alloys for the manufacturing of microchannel-based hydrogen storage thermal management systems.

3.4 Objective

The objective of this thesis is to determine whether laser welding and heat treating strategies can be developed for a 6061 aluminum microchannel cooling plate as part of a larger hydrogen storage thermal management system. Key manufacturing process requirements include controlling the hermeticity, strength and dimensional stability of the heat-treated weld joint. To demonstrate functionality of the cooling plates, the resulting laser-welded cooling plates are evaluated based on cooling capacity and pressure drop.

4. Experimental Approach

The objective of the current study is to obtain a set of laser keyhole welding and heat treatment parameters for producing precipitation-hardened aluminum cooling plates with hermetic joints, high weld strength and minimal warpage. The weld lap joint needs to have a weld depth roughly equal to the thickness of the two plates and be free of defects such as porosity, solidification cracking and voids among others which can reduce the strength of the joint. The strength of the joint should be able to sustain the forces acting on it without failure or leakage in the joint.

4.1 Prototype Cooling Plate

A cooling plate was designed in order to investigate key welding requirements and ultimately to test the functionality of the device. The 30 cm liquid nitrogen cooling plate design (see above) was scaled down to a 5 cm diameter cooling plate prototype. The top lamina was 500 μm thick with channels photochemically machined to a depth of approximately 250 μm. The top lamina was 250 μm thick with inlet and outlet ports photochemically machined to a diameter of approximately 2 mm.

In order to withstand 50 atmospheres of hydrogen, it was necessary to control the distance between support pillars. Based on previous FEA and using a factor of safety of 1.6, the span between support pillars was reduced to 1.93 mm. The thickness of the plates, channel depth, size of support pillars and flow directors were made the same as in the original design. The welding bosses were spaced equidistant in a circular pattern with the distance between circular patterns equal when measured from the

circumference except the welding boss at the center. Additional space was provided around the periphery of the 5 cm device for clamping and alignment of plates during laser welding. The final cooling plate design is shown in Figure 11.

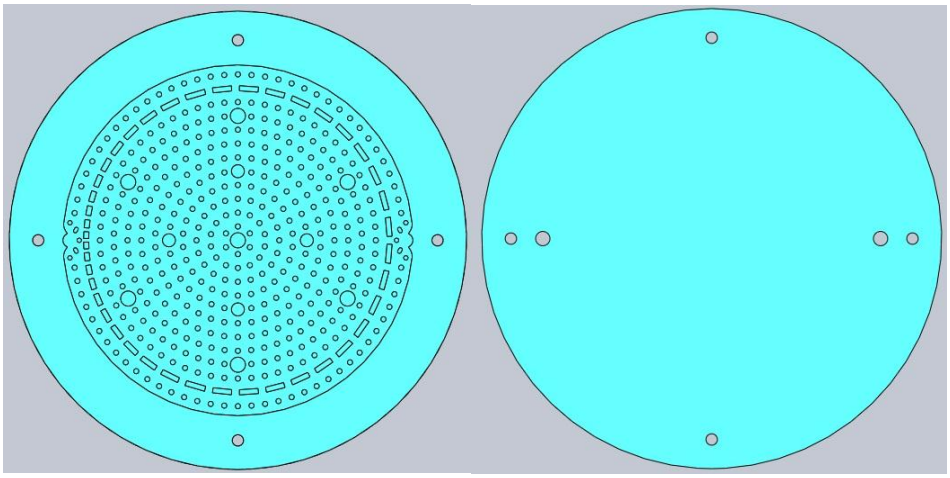

Figure 11: Cooling plate prototype: (left) bottom lamina; and (right) top lamina.

In order to operate at heat fluxes required of the 30 cm cooling plate (1.14 W/cm^2), the prototype cooling plate was designed to remove 22.4 W. The flow rate of water required to remove the heat was calculated using a simplified model, Q=mCpdT, where dT is assumed to be 7 K. The minimum flow rate required 46 ml/min.

The cooling plate includes variable cross sectional area in the flow direction, variable pillar diameter for flow distribution leading to variable flow distribution of the flow in the cooling plate. None of the existing theoretical models available are able predict the pressure drop and the heat transfer characteristics through the plate. Three dimensional computational fluid dynamics (CFD) simulations were performed using ANSYS Fluent to predict the heat transfer behavior of the cooling plate.

CFD simulations were performed on the cooling plate with the flow rate of 200 ml/min and a heat load of 22.4 W on one surface. Figure 12 shows the CFD simulation for velocity magnitude of the flow. The velocity of the flow is found to be uniform over the plate except at the inlet and the outlet.

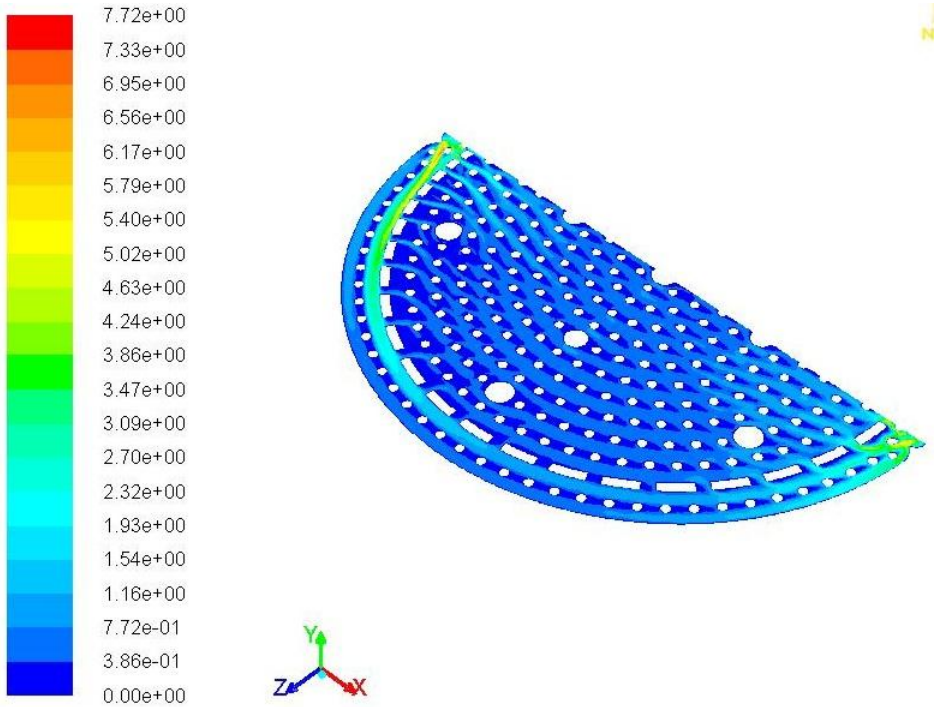

Figure 12: CFD simulation showing velocity magnitude of flow. (Courtesy of Daniel Peterson and of Eric Truong)

Figure 13 shows the total temperature profile in the cooling plate. The fluid enters the cooling plate at room temperature and gains heat over the flow area and leaves the cooling plate at higher temperature. The heat removed from the cooling plate was calculated using the inlet and outlet temperature, the heat removed was found to be equal to heat supplied. This shows the ability of the cooling plate to remove the heat from the surface. Thus, the CFD simulation validates that the prototype design provides a uniform flow and heat removal throughout the cooling plate.

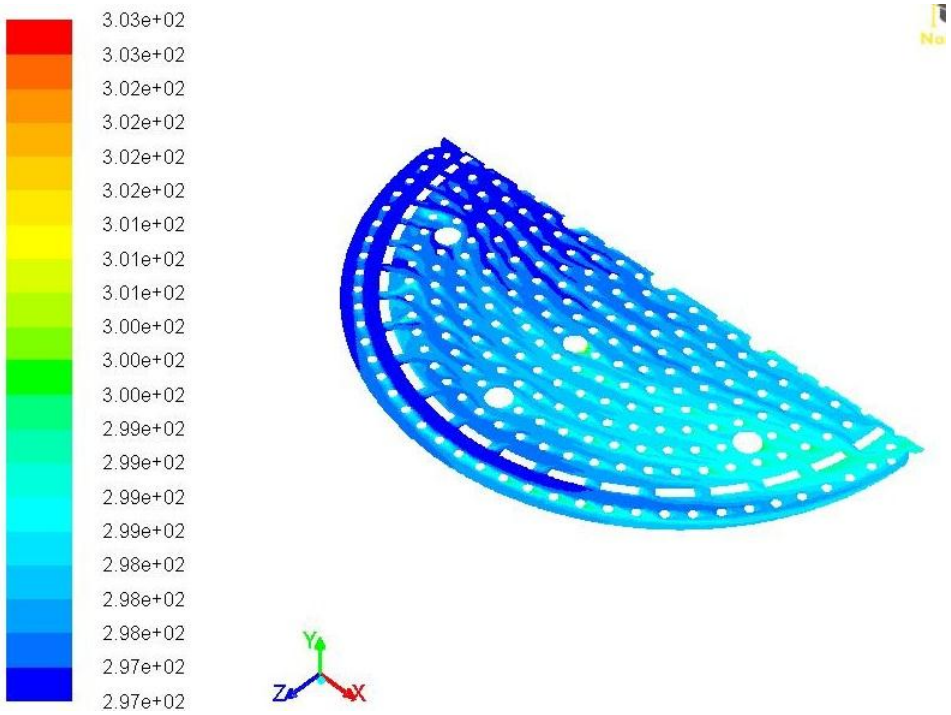

Figure 13: CFD simulation showing total temperature of flow. (Courtesy of Daniel Peterson and of Eric Truong)

High pressure drop is observed at the inlet and the outlet of the cooling plate due to a 90 degree bend in the flow direction and a rapid change in the flow area. The highest pressure drop of 0.37 atm was found at the inlet.

4.2 Laser Welding Setup

All experiments were conducted on a Rofin F010 S: single mode, continuous wave Yb-fiber laser with fiber diameter of 20 µm. The wavelength of the beam is 1080 nm, beam quality of 0.4 mm-mrad and maximum power of 1000W. A minimum beam diameter of 28 µm was obtained using a collimator lens. In this the thesis, the laser setup was operated in a galvanometer mode where the workpiece is kept

stationary and the beam moves. The work area for galvanometer mode welding is limited due to the size of the optics.

The workholding clamp used in the current study is shown in Figure 14. The test article was placed between the top and the bottom platen using alignment pins for proper alignment. The top and bottom platens were pressed together using a toggle clamp. A screw on the toggle clamp was used to vary the distance between the top and bottom platen. The desired clamping pressure was obtained by considering the compression of a gasket. Inlets in the top platen provided for shielding gas during welding. The gasket and platens were replaceable. The clamping system shown in Figure 14 was used to produce simple 25.4 x 25.4 mm rectangular test articles for preliminary experiments and some primary experiments. In the following sections, rectangular test articles that were welded within this clamp design are sometimes referred to as design A.

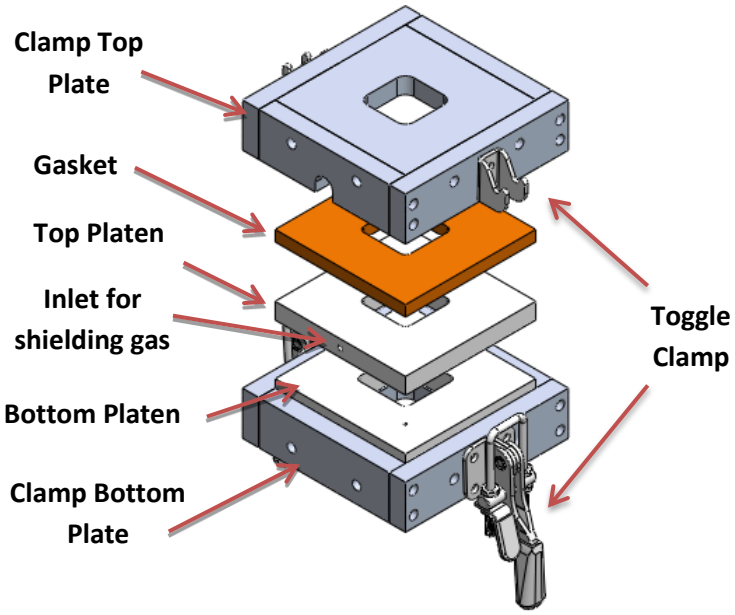

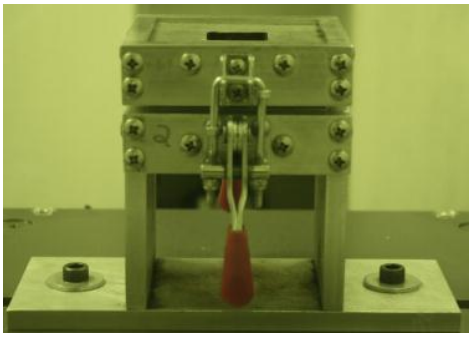

Figure 14: Clamp for laser welding (Courtesy: Design by Mark McGuire; Design modification by Sam Brannon and Steve Etringer)

In order to accommodate the cooling plate design, the gasket and platen assembly was modified as shown in Figure 15. The top platen was modified as shown in Figures 15a and 15b to help in distributing inert gas to the welding zone during welding. All platens and gaskets included a 5.33 cm diameter circular hole to provide laser access to the cooling plate for welding a circular weldment 5 cm in diameter. As shown in Figure 15a, the modified top platen included a 2.54 mm wide groove for distributing shielding gas to the welding zone. The modified top plate assembly was sealed using a thin gasket and a cover plate as shown in Figure 15b. The shielding gas flowed through the axial inlets provided on the clamp cover plate (Figure 15c) and was distributed through the groove to the weld line as shown in Figure 15a. The cover plate and the top plate were assembled together using screws forming the top platen assembly. Below, test articles produced in this clamp are sometimes referred to as design B.

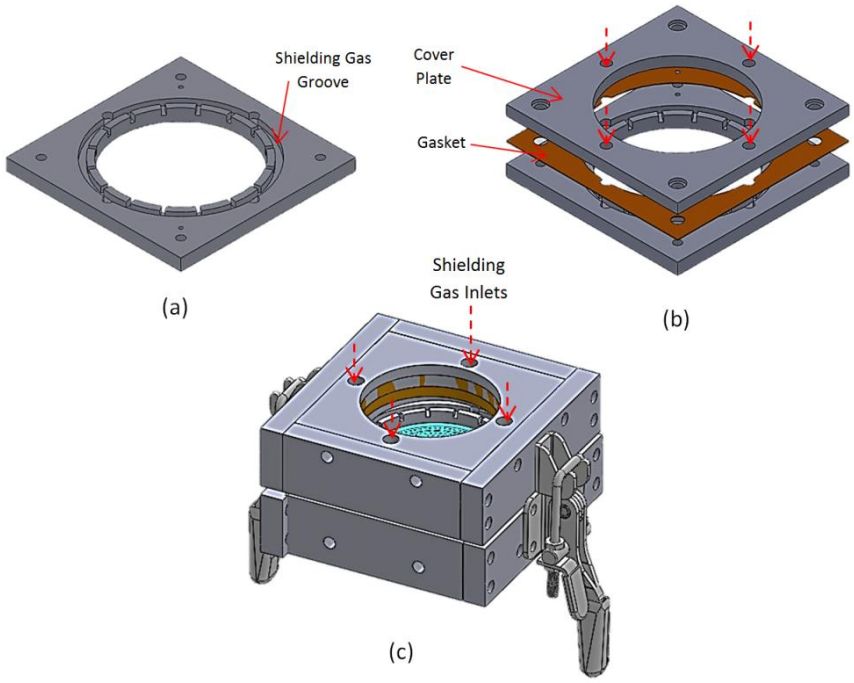

Figure 15: Modified clamp design: (a) modified top platen; (b) modified top platen assembly; and (c) assembled cooling plate clamp showing shielding gas inlets.

4.3 Hermeticity Testing

The most difficult requirement to meet in this thesis was hermeticity. Therefore, this requirement was the first to be investigated. The objective of the hermeticity experiment was to determine the welding conditions necessary to produce a hermetic seal for the cooling plates. A hermetic testing clamp was designed and fabricated to test the hermeticity of design B test articles as shown in Figure 16. The clamp consisted of top and bottom platens providing the necessary pressure to seal the test articles using o-ring at the inlet and outlet ports on the top plate. Prior to testing, the welded test article is mounted within the hermeticity clamp. The inlet port is connected to an air regulator connected to line air and the outlet port is plugged. The assembly is submerged in water to observe any leakage. The air pressure is gradually

increased up to a maximum of 100 psi and kept at that pressure for 15 minutes. The test article passes if no air bubbles are seen coming out of the cooling plate.

Figure 16: Hermeticity clamp for cooling plate prototype

A continuous circular weld was initially tested on a 55 x 55 mm square test article consisting of two 0.5 mm thick 6061-O laminae laser welded using the clamp arrangement for design B and using galvanometer mode laser welding. A power ramp was used at the start and end of the weld to avoid the blowout of metal due to the ramp up and down of the laser scan. More details on these defects can be found in Appendix C1. Initially, a wide range of parameters were tested from high power to low power. The parameters tested were designed to produce a partial penetration weld approximately halfway into the bottom foil. These parameters and their measured weld depth are shown in Table 3 below.

Table 3: Parameters for laser welding two 0.5mm thick plates

Power (W)	Speed (mm/s)	Weld depth (mm)
1000	650	0.76
900	550	0.756
800	500	0.756
700	400	0.752
600	300	0.787
500	200	0.796

4.4 Warpage

Preliminary experiments were conducted to investigate methods to reduce warpage in the cooling plates primarily due to heat treatment. During laser welding a very high amount of heat flux is induced in the material. This heat melts the material and the material expands. Part of the heat is conducted to adjacent metal which does not reach a temperature high enough to melt the metal. When the laser is withdrawn from that area, the molten metal contracts which can lead to thermal warpage and even cracking. When performing a circular weld on the cooling plate, the top of the plate deflects concavely. The warpage in the cooling plate was measured by evaluating the parallelism of the plate.

Further, the cooling plate is then subjected to a solution heat treatment and quenching. During quenching, thermal gradients lead to non-uniform contraction of the metal and warpage. Appendix D explains the methods used to reduce warpage in the aluminum test articles. Experiments were conducted on aluminum test articles using different quench media in order to evaluate their effect on test article warpage. It was concluded that free convection in air induced the least amount of warpage in the material.

A flattening cycle was performed on the cooling plates consisting of heating the cooling plates up to 350ºC and applying 10 MPa of pressure for 1 hour. After cooling, the plates were measured for flatness individually. The cooling plates were then laser-welded (using the conditions above), solution heat treated and quenched by free convection in air. Solution heat treatment was performed at 565 °C for 35 minutes.

Afterward, the cooling plates were allowed to cool under equilibrium conditions in air. The shims were then subjected to an artificial aging process at 160°C for 18 hours.[45]

Warpage in the cooling plates was measured both after welding and after heat treatment using a ZeScope Optical Surface Profiler by Zemetrics Inc. To measure warpage, the material was placed on the ZeScope datum having a flatness standard deviation of ±3 μm and the height of the plate top surface was measured. The beam was focused at the center of the cooling plate which acted as the reference point for other measurements on the plate. The height of the cooling plate was measured at several places represented in Figure 17 as the intersection of the radial lines and circles. A total of 41 measurements were made on each plate; five on each radius as shown in Figure 17 and one at the center. Figure 18 shows the set-up of the ZeScope for warpage measurement. Three cooling plates were used to evaluate the cooling plate warpage due to laser welding and heat treatment.

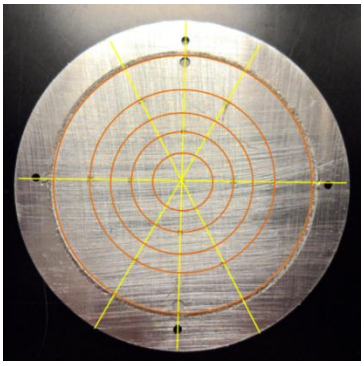

Figure 17: Location of measurement on the welded samples

Figure 18: ZeScope for warpage measurement

4.5 Weld Strength

Experiments were conducted to evaluate the strength of the welded joints using the hermetic laser welding and precipitation hardening heat treatment conditions established above. The main objective of the experiment was to evaluate the joint strength of the welded joint.

Lap shear test articles [72] used in the study consisted of two rectangular shims overlapping at the edges as shown in the Figure 19. A line was welded on the overlapping region using clamp design A. Lap shear tests were performed on a 5969 Dual Column Tabletop Universal Testing Systems with a strain rate of 0.5 mm/s. The weld length and width at the interface was calculated after failure for weld strength calculations.

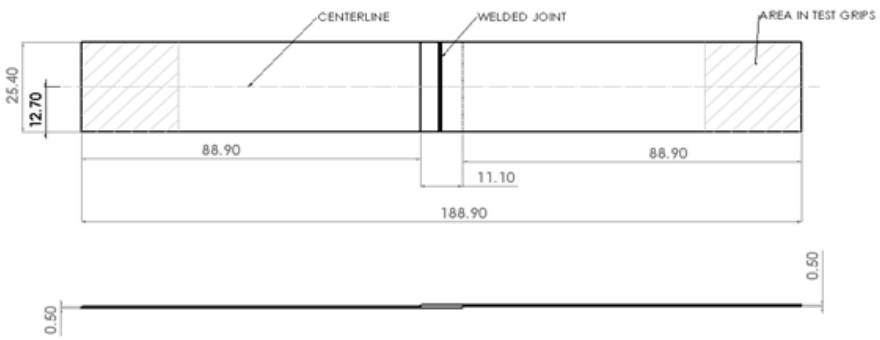

Figure 19: Lap Shear Test Article

4.6 Functional Evaluation of Cooling Plates

The objective of this experiment was to evaluate the ability of the cooling plates to remove the heat load that they were designed to remove at a given flow rate with acceptable pressure drop through the channel. The cooling plate prototype in Figure 12 was designed to remove 22.4 W of heat from one surface of the cooling plate. The working fluid used in this experiment was water. The minimum flow rate required to remove the heat supplied

Figure 20 shows a block diagram of the experimental setup used to evaluate the cooling capacity and the pressure drop through the cooling plate. The setup was designed to incorporate water as the working fluid.

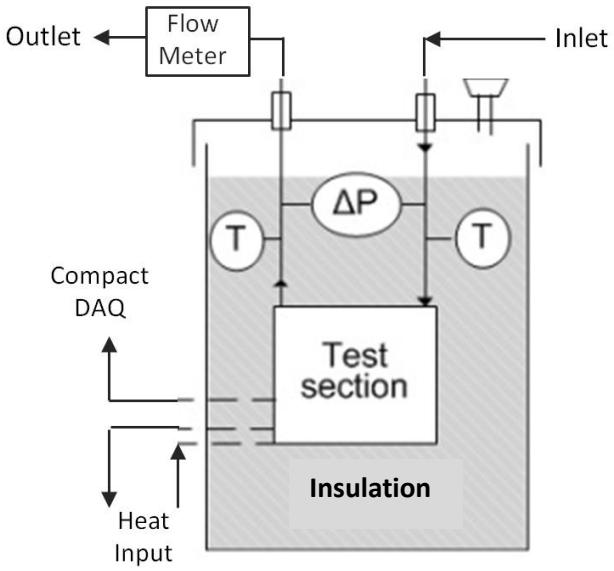

Figure 20: Experimental setup for evaluating the functionality of the cooling plate. (Courtesy of Erfan Rasouli and Professor Vinod Narayanan.)

Figure 21 shows the experimental setup for the cooling capacity test. The liquid flowed through the cooling plate and, after exiting, through the flowmeter to measure flow through the system. Pressure drop through the cooling plate was measured using a pressure transducer connected to the inlet and outlet of the flow channel. A small port was used at the inlet and the outlet of the system to connect a pressure transducer to measure the differential pressure between the inlet and the outlet. The port for the pressure measurement was approximately 10 cm above the inlet/outlet of the microchannel. The pressure drop from the inlet/outlet to the pressure transducer were calculated and found to be very small. The pressure transducer and the flow meter were calibrated prior to the experiments. The thermocouples were specified to measure the temperature with a calibration error of ±0.3 K.

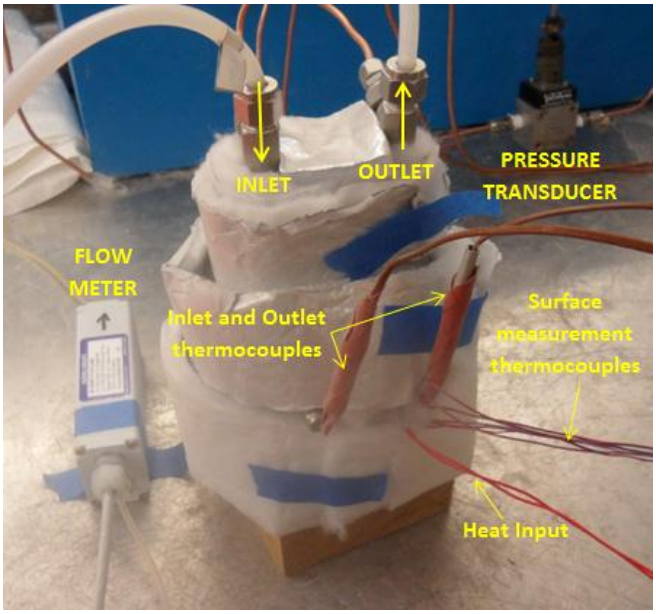

Figure 21: Experimental setup for cooling capacity of cooling plates

A heat load of 22.3 W was applied to the cooling plate using a Kapton heater. A heater of 5.08 x 5.08 square cm with adhesive backing was adhered to the bottom of the cooling plates. Thermocouples were placed at six positions on the cooling plate to record the temperature of the cooling plate using compact DAQ. Figure 22 shows the location of the thermocouples, one near the inlet and outlet and four at the circumference. The temperature of the liquid was measured before entering and after exiting the cooling plate. The cooling capacity and the flow distribution of the plates were evaluated based on the ability of the cooling plate to remove the applied heat load and the temperature uniformity across the cooling plate.

All the thermocouples were placed at a radius of 10 mm from the center of the circle and at an equal angle from each other. Thermocouple 2 measured the temperature of the incoming liquid and thermocouple 5 measured the temperature of the outgoing liquid. Thermocouples 1 and 3 measured the temperature of the liquid at

the inlet side of the cooling plate and thermocouples 4 and 6 measured the temperature at the exit side of the cooling plate. Temperatures for thermocouples 1, 3, 4 and 6 provide data regarding the distribution of the flow (and therefore temperature) in the cooling plate.

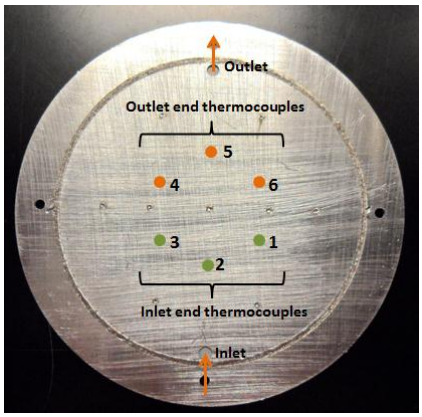

Figure 22: Position of thermocouples on the cooling plate.

Experiments were performed on the cooling plates in terms of heat removal capacity, pressure drop and flow distribution for different flow rates of water. The heat removed from the cooling plate was determined by the following equation: $Q = \dot{m}C_p\Delta T$, where, Q is heat removed, ΔT is differential temperature between inlet and outlet of cooling plate, $\dot{m}$ is mass flow rate and Cp for water is 4.187 J/kg.K

5. Results and discussions:

5.1 Hermeticity

Test articles were tested for hermeticity using the parameters shown in Table 3. Initially, none of the parameters were found to produce hermetic weld joints. Visual inspection of the welds showed that the higher welding speed creates instabilities in the keyhole leading to blowouts and splashing of the molten metal as shown in Figure 23. This creates voids at the regions where the metal is blown out leading to leakage through the top of the weld. High welding speeds and shielding gas flow rates were determined to be the major cause for this phenomenon. At 20 liters/min of shielding gas, these defects were predominant at welding parameters above 600 W and 300 mm/s. When the shielding gas flow rate was reduced to approximately 5 liters/min, these defects were minimized at laser welding parameters of 700 W and 400 mm/s and below.

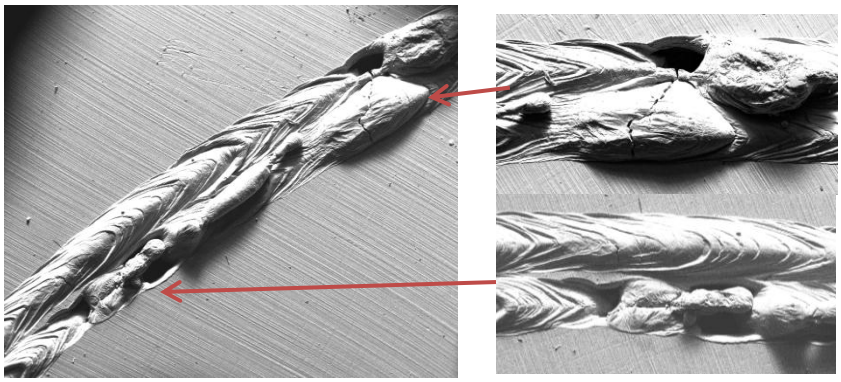

Figure 23: Instabilities in weld seam

To further reduce the occurrence of keyhole instabilities, the weld path was shortened to reduce the length of time required for keyhole stability. The new weld

path is shown in Figure 24 and consists of two half circles overlapping at the interface to form a full circle.

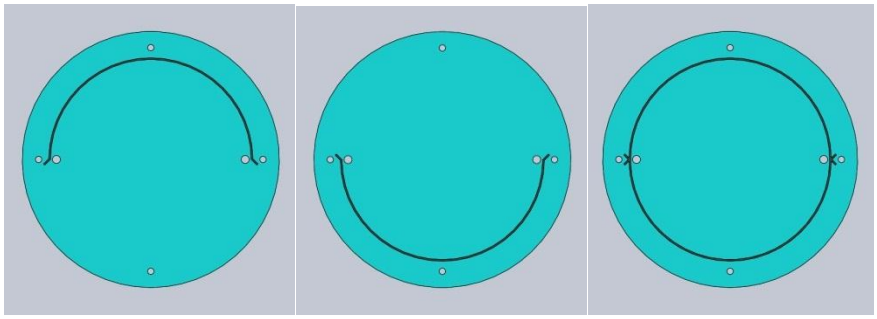

Figure 24: Weld design for hermeticity

The new weld paths were used to produce square test articles using the welding conditions for power levels between 400 and 700 W described in Table 3. While no leakage was observed on the top of the weld and the rate of leakage overall was reduced significantly, none of the welds were found to be hermetic. To diagnose the cause of failure, a pressurized dye was injected into the test articles and the welded joints were forcibly opened revealing the fracture surfaces for visual inspection.

Solidification cracking and porosity were found to be the two major defects at the weld interface. At higher laser powers (600 and 700 W), cracking was found to be the dominant phenomenon responsible for leakage. Porosity was observed in some joints but these failures were fewer in number. Figure 25 shows a microscopic image of cracking observed at the weld interface. In addition to causing leakage, these cracks were expected to reduce the strength of the joint considerably.

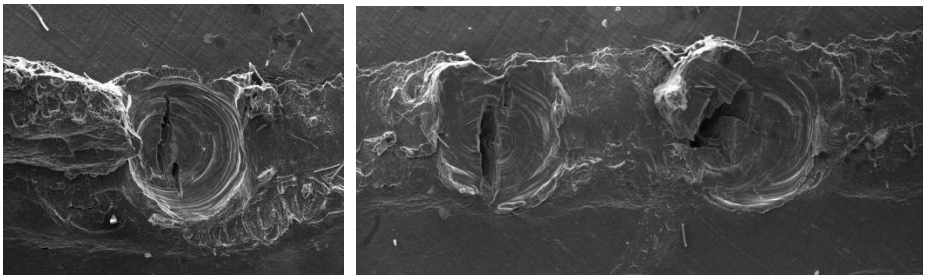

Figure 25: Solidification cracks at the interface of the welded joint

Lower laser powers (400 and 500 W) yielded considerably less joint leakage. Very few cracks were observed at the weld interface. Figure 26 shows evidence of porosity at the weld interface despite the use of shield gas. In addition, the width of the weld line seems to have large variability. To improve the hermeticity of these lower power weld joints, full penetration welds were pursued. The logic was that full penetration welds would provide a larger weld interface and minimize the effects of weld width variability. Full penetration welds (1 mm weld depth) were produced on square test articles using 500 W power and 80 mm/s. Good hermetic seals were obtained using these welding conditions.

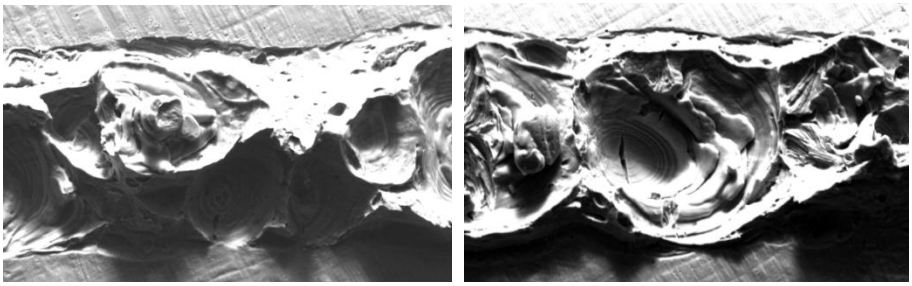

Figure 26: Evidence of porosity at the weld interface.

Consequently, low wattage (500 W) full penetration welding conditions were developed for the prototype cooling plate. Full penetration welding for the cooling plates required a weld depth equal to a combined thickness of 750 µm for the two halves of the welding plate. Initially, welding parameters of 500 W and 200 mm/s

were used while focusing the beam 200 µm into the substrate (i.e. a 200 µm defocus). Weld instabilities were found under these conditions. It was hypothesized that this was perhaps due to the nearness of the focal plane to the weld interface (i.e. the top plate of the cooling plate was 250 µm in thickness). Hence, the defocus was reduced to 50 µm. The decrease in the defocus reduced the weld depth obtained and hence the weld speed was decreased to 180 mm/s. As before, power ramps were used at the start and end of the weld lines in order to control weld depth and blow out at the start and end of the welds. Argon was used as the shielding gas.

Three test articles were laser-welded, heat-treated and tested at similar conditions to investigate repeatability of the process. All three cooling plates were found to be hermetic with no leaks when tested up to 100 psi of air pressure.

5.2 Warpage

The cooling plate laminae were evaluated for parallelism prior to joining and heat treatment and the parallelism of the plates were found to be ± 8.5 µm. Figure 27 shows the average change in distance from the surface of the plate with standard error bars as a function of distance from the center of the plate for two conditions: 1) after welding; and 2) after heat treatment. The graphs were plotted with respect to the center of the plate which was found to be the lowest point on each plate. The largest component of warpage was found to be due to laser welding.

Warpage due to laser welding was expected and is due to the contraction of the heated and molten metal adjacent to the weld zone.[70] The maximum warpage is at the outer end of the cooling plate where the material is joined together using laser

welding. Regarding the effect of heat treatment, it is expected that the thermal profile annealed the plate reducing its mechanical properties and thus causing the stresses due to the material contraction to have a larger effect on the plates.

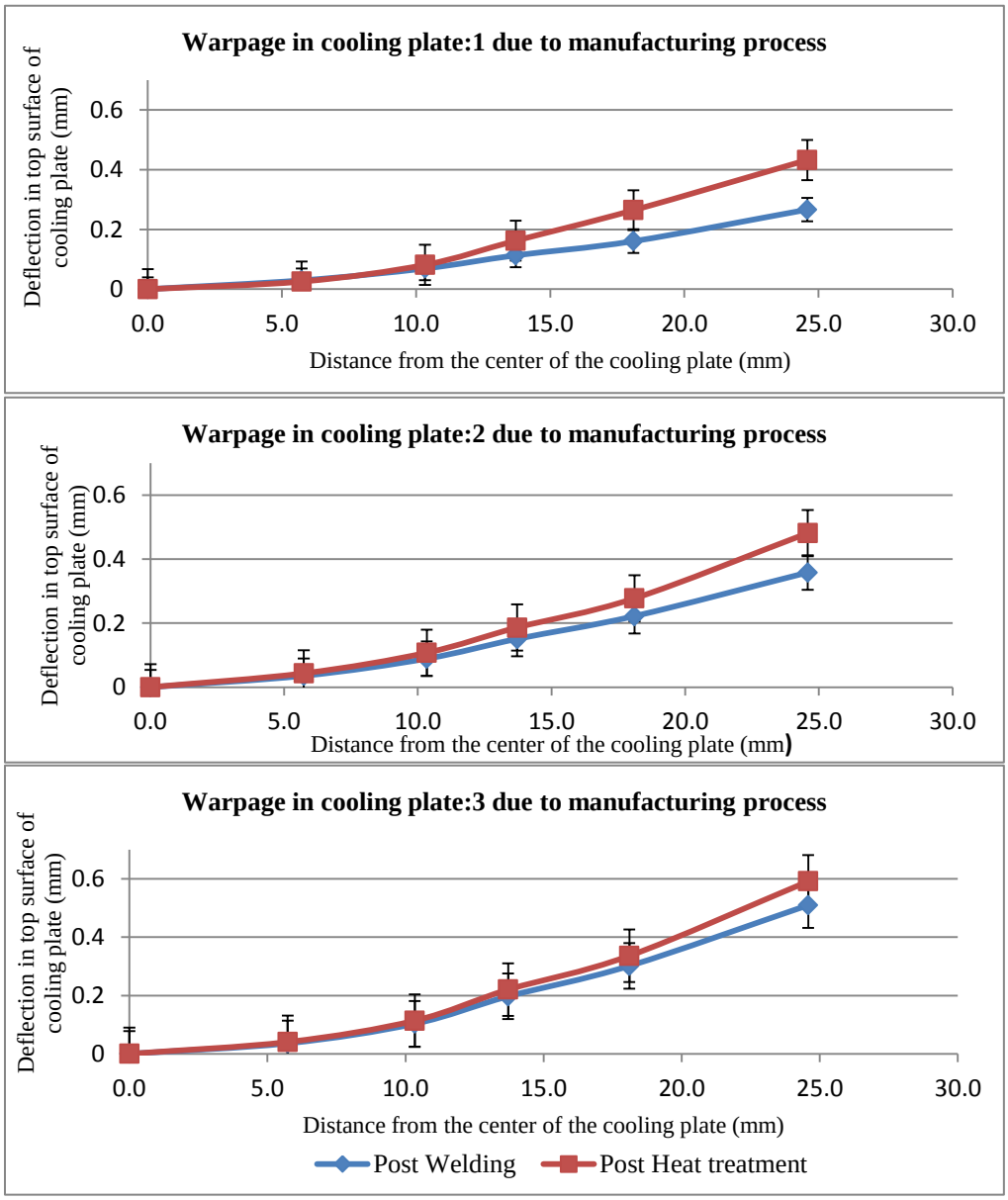

Figure 27: Warpage in cooling plates

The results in Figure 27 suggest that the gap between the adsorption media and the cooling plates may be as large as 0.5 mm in the center which is approximately one

percent of the overall bed height assuming two 2.5 cm high adsorption modules per plate. Further, it is expected that once assembled, this gap will be significantly smaller due to the cooling plate being under compression. Finally, it is expected that this gap will not be a significant issue particularly when considering that it will be filled by hydrogen at 50 bars of pressure which has a high thermal conductivity.

A more important defect is the deflection of the microchannels within the cooling plate leading to flow maldistribution. To investigate this, the welded cooling plates were dissected in order to investigate the microchannel cross-sections. Figure 28 shows some cross-sections of microchannels within a cooling plate. The microchannel height was measured at several places and the average height of the channel was found out to be 266.4 μm with a standard deviation of 10.7 μm providing a 4.0% coefficient of variation (COV). COVs below 5.0% have been found to have minimal impact on the flow misdistribution and effectiveness of microchannel heat exchangers.[37] Further, it was found that the majority of this variation was due to the etch depth tolerances (272.5 μm, COV of 4%, Appendix C) of the photochemical process than the warpage of the microchannel fins. Photochemical machining of aluminum alloys require high etch-depth tolerances due to the compositional differences in material from lot to lot and the high density of the features which can make etchant access through the photoresist to the material surface difficult. This suggests that the tolerances provided via laser welding and heat treatment is acceptable for producing 6061-T6 aluminum microchannels.

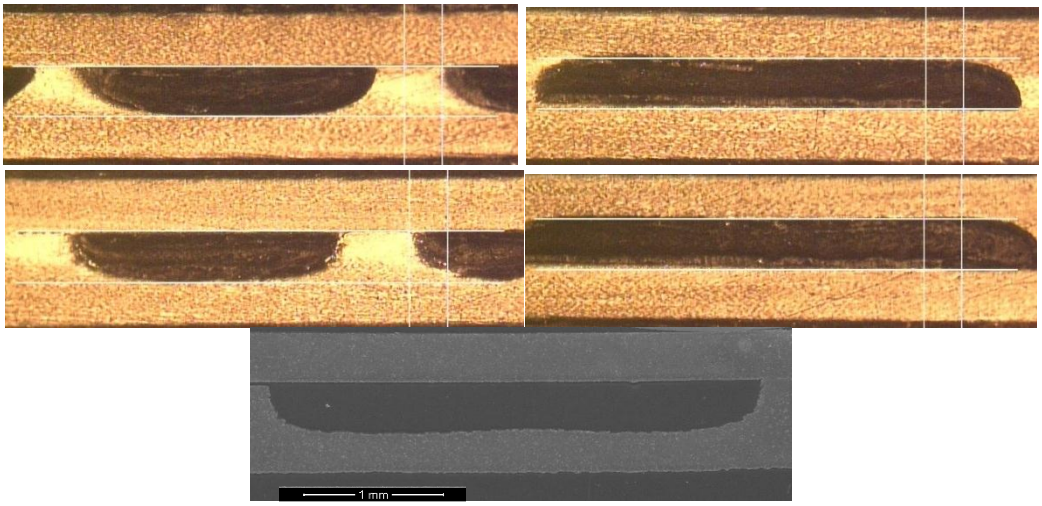

Figure 28: Cross section of cooling plate

5.3 Weld Strength

Lap shear test articles were produced using the same laser welding and heat treating conditions described above. Tensile test articles were cut out of the base material and heat treated under the same conditions. Lap shear tests were conducted on the welded test articles and tensile tests were conducted on the base material test articles.

Figure 29 shows the tensile strength in shear and yield strength in shear of the laser-welded aluminum alloy and the base metal. For comparison between the base metal strength and weld joint results, the approximate yield and ultimate strengths in shear of base metal can be obtained by multiplying the values by 0.65. [71] The base metal tensile strength obtained was 202 MPa, which corresponds to the expected strength of the 6061-T6 aluminum alloy. The yield strength of the base metal was 173 MPa which is slightly lower than the expected strength of 179.4 MPa.

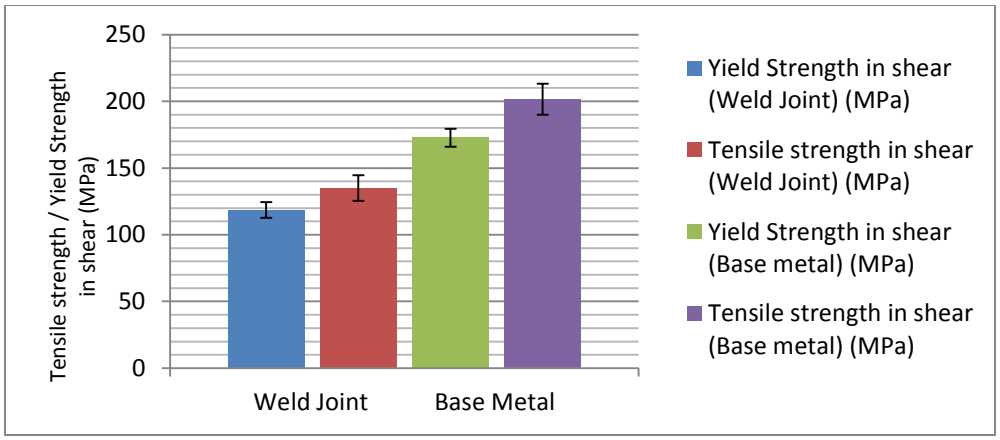

Figure 29: Base metal strength and weld joint strength in shear

The yield and ultimate strengths of the laser weldments in shear were 118.5 and 134.9 MPa, respectively, which are 68.5% and 66.8% of the base material strength, respectively.

Fractography was performed on the lap shear test articles to determine the mode of failure. It can be observed from the cup and cone structures in Figure 30 that the failure occurred predominantly in the ductile mode. Voids and porosity can also be observed in the fractured surface as shown in figure below.

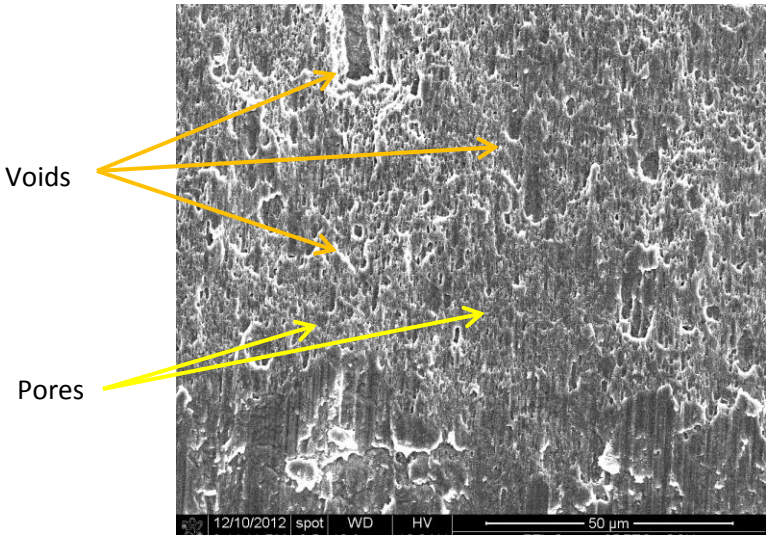

Figure 30: Fractography of a laser-welded lap shear coupon.

Figure 31 shows a cross-section of the welded joint. It can be observed that the precipitates in the weld zone are coarser than the precipitates outside the weld zone. This difference in the size of the precipitates is the major reason for differences in the strength of the base metal and the weld joint.

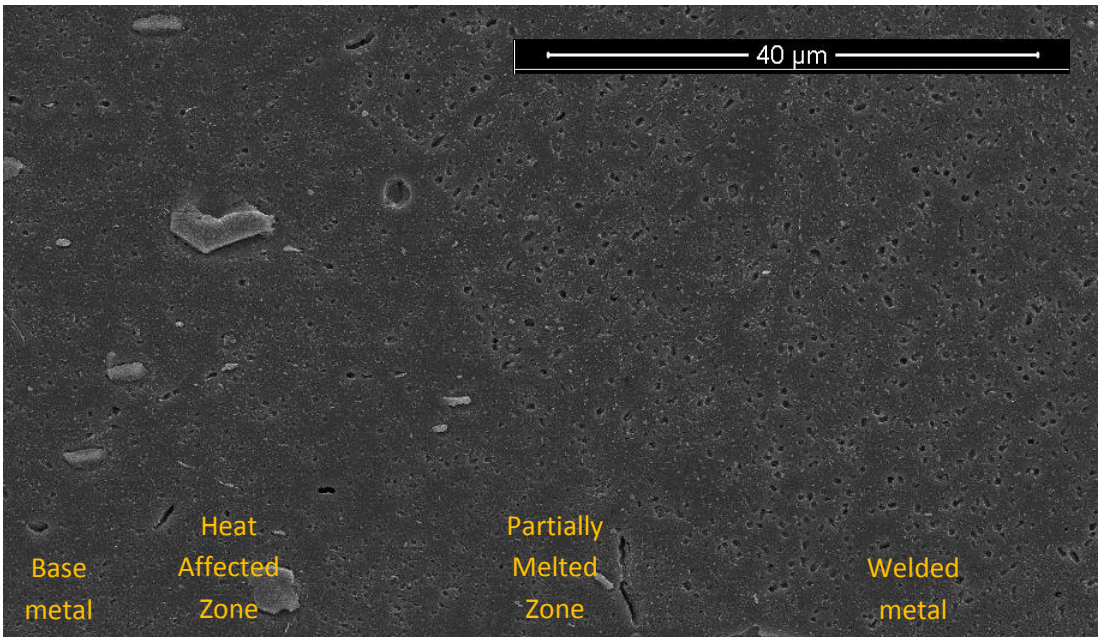

Figure 31: Microstructure of interface of welded joint and base metal

Another reason for the reduction in the strength of the weld joint may be due to depletion of Mg in the heat affected zone. To evaluate the loss of alloying elements in the weldment due to laser heat input, Wavelength-Dispersive X-Ray Spectroscopy (WDS) analysis was performed on welded joints produced at 500 W and 200 mm/s. The alloying elements measured in the test were aluminum, magnesium, and silicon. Mg_2Si is the strengthening element in 6061 aluminum alloy and Mg is more susceptible to evaporation during the laser welding leading to reduced strength. Figure 32 shows a WDS analysis measurement line across a portion of the joint. The analysis shows that the laser welding did not lead to significant loss of silicon from the material. Magnesium depletion was measured be around 6% of amount of magnesium found in the base metal. It is expected that this small loss of magnesium does not lead to huge reduction in the strength of the weld joint. Additional WDS analyses were performed for joints formed at 900 W and 1000 W showing similar results. No evidence was found to support Mg depletion as a plausible factor affecting weld strength.

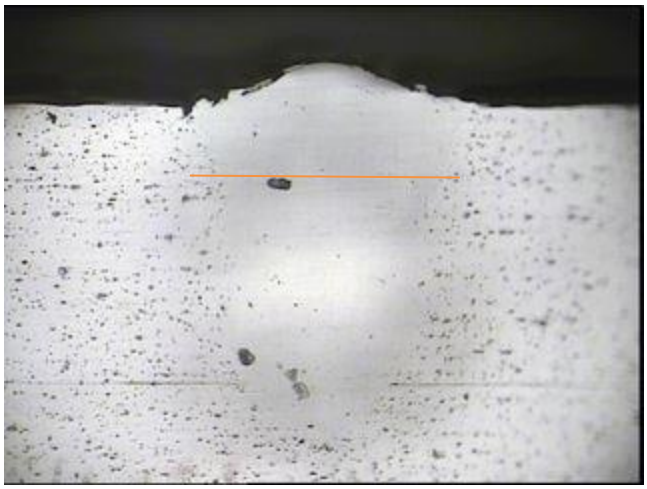

(a)

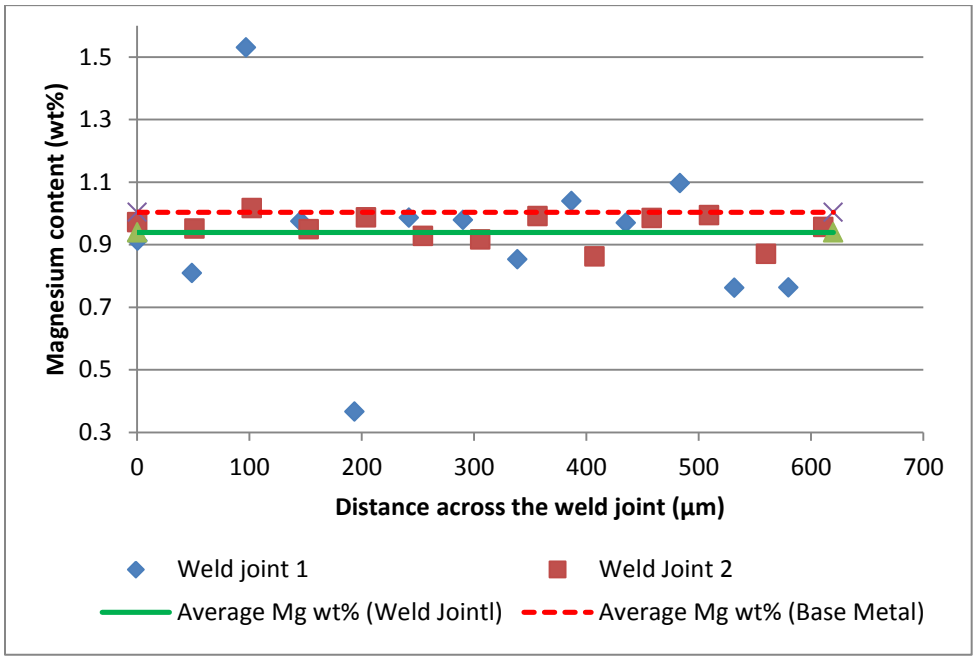

(b)

Figure 32: WDS analysis cross section (a) Cross section showing location of measurement; (b) Magnesium content in wt. % across the weld joint

To investigate the effect of the heat treatment, microstructures of laser welded joints quenched in water and air were observed under SEM. Figure 33(a) shows the microstructure of the weldment quenched by free convection in air and Figure 33(b) shows the microstructure of the weldment quenched in water. It can be observed that

the dark features observed in the weldment quenched in water are smaller in size as compared to the weldment quenched by free convection in air. Since the only difference in these pictures is the heat treatment, this indicates that the dark features are precipitates and not pores. The coarser size of the precipitates in the weldment quenched by free convection in air explains the reduction in the strength of the weldment.

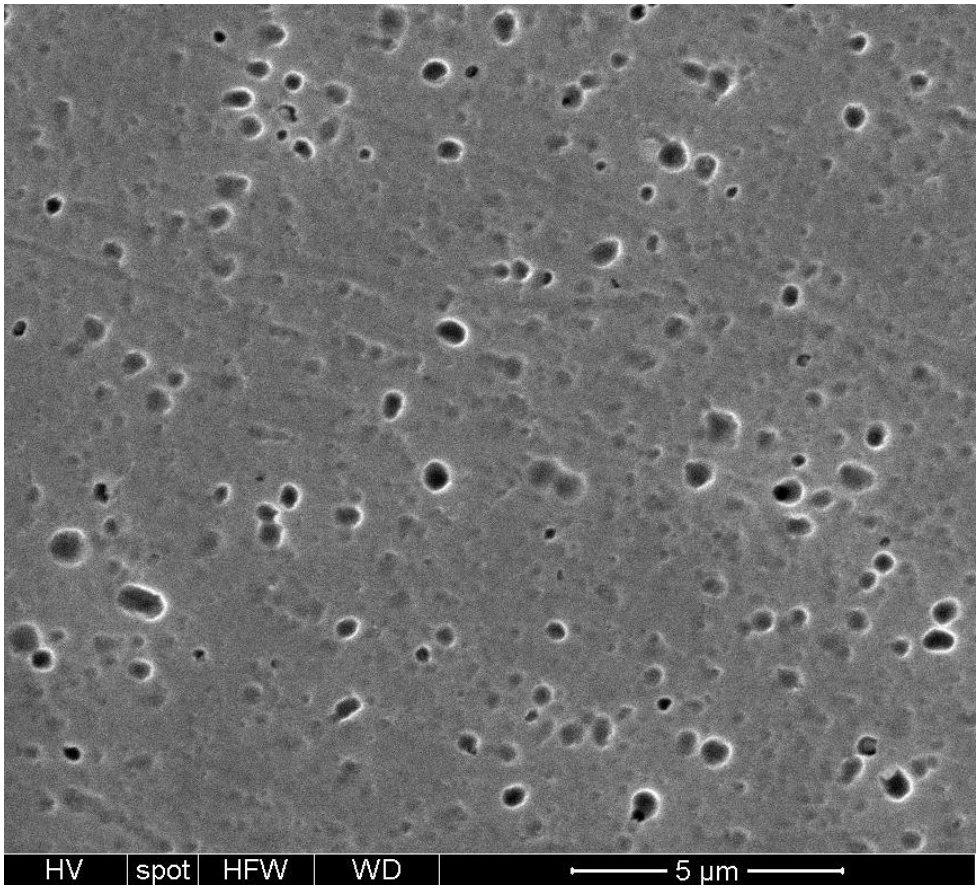

Water quench

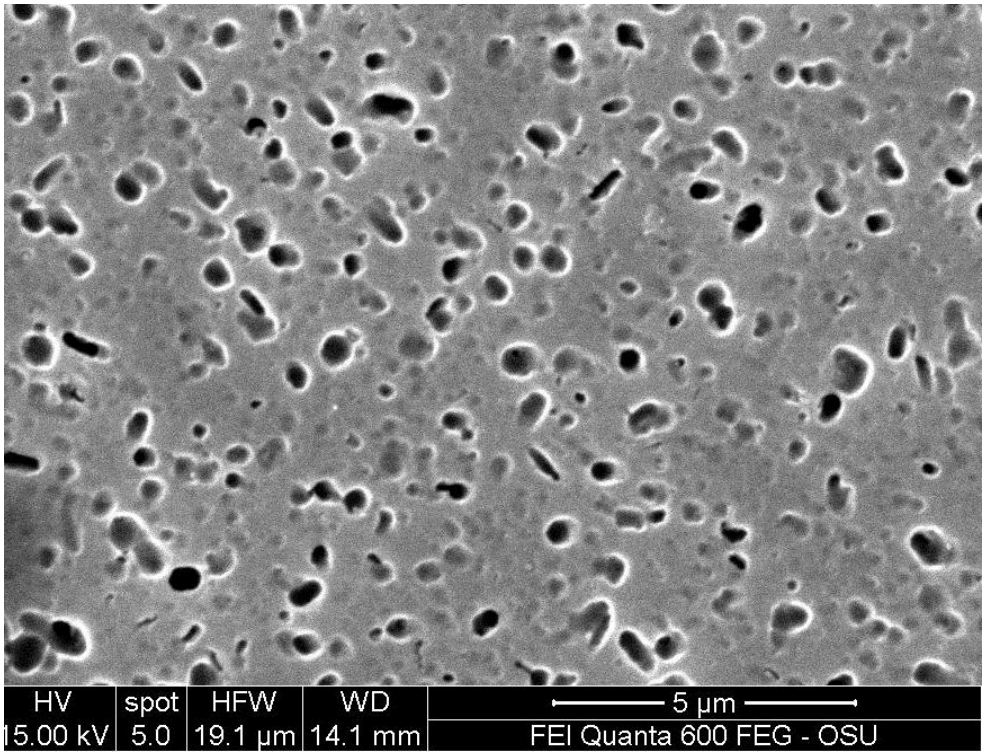

Air quench

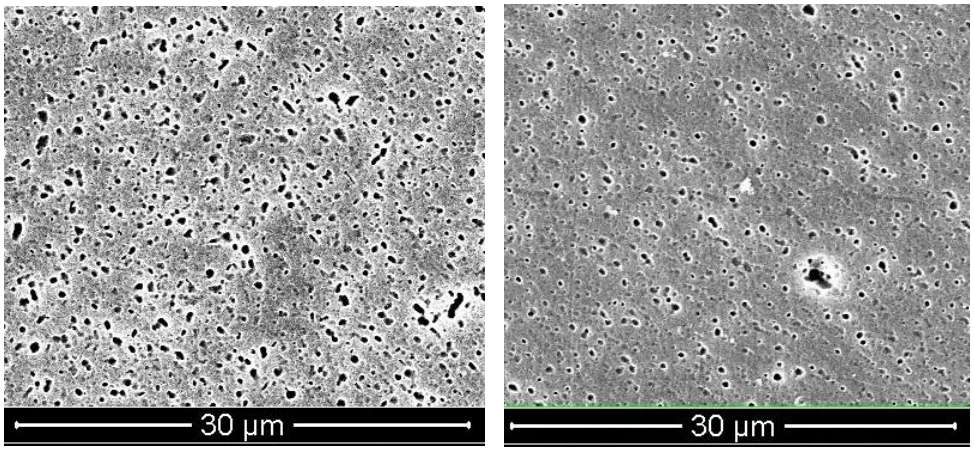

(a) (b)

Figure 33: Microstructure of the weld zone for weldments quenched (a) in air and (b) in water.

5.4 Functional Evaluation of Cooling Plates

Figure 34 shows the heat removed by the cooling plates at different flow rates. The minimum flow rate required for removing the heat load of 22.4 W was determined to be 198 ml/min. At 50 ml/min and 198 ml/min, the experimental percent error with CFD calculations was found to be 13.4% and less than 1% respectively. This variation is likely due to heat losses to the surrounding based on the high conductivity of aluminum.

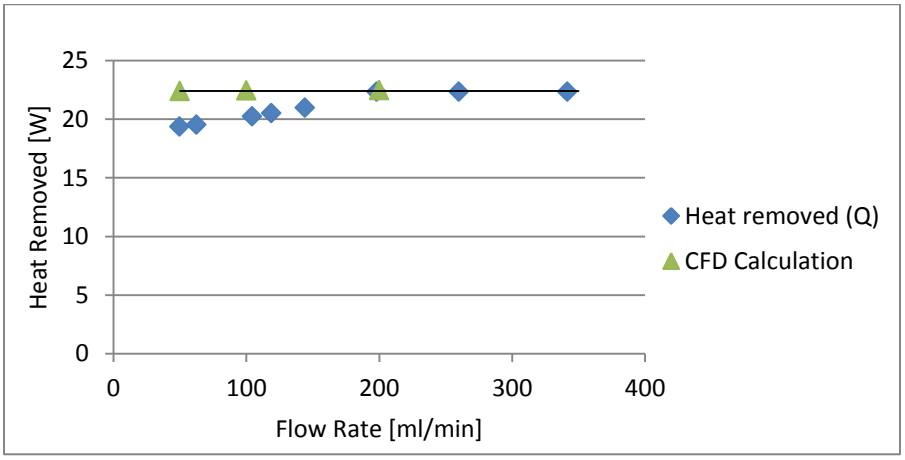

Figure 34: Heat removed at different flow rates (CFD Results: Courtesy of Eric Dang)

Figure 35 shows the change in pressure drop across the cooling plate at different flow rates. As shown, the pressure drop through the cooling plate increases with flow rate. A trend line was developed based on experimental results. The pressure drops obtained at 200 and 260 ml/min appear to be outliers. Therefore, these points were omitted from the trend line. The average experimental error when compared to CFD results was found to be 25% based on the trend line. It is expected that this variation in results may be due to frictionless flow assumptions made in the CFD model.

Pressure drop accuracy appears to improve at higher flow rates with the error reducing below 10% at 200 ml/min.

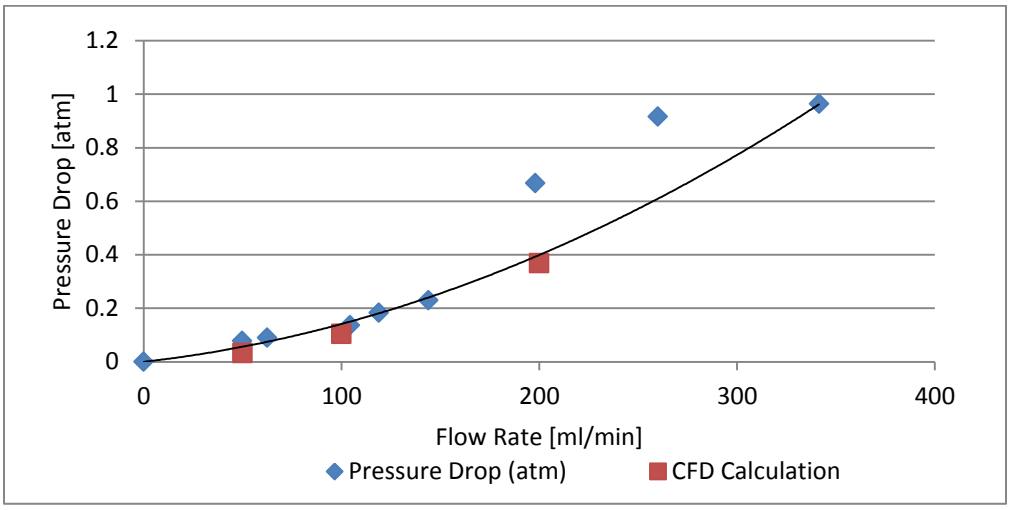

Figure 35: Pressure drop at different flow rates (CFD Results: Courtesy of Eric Dang)

Flow distribution was evaluated by the use of thermocouples across the cooling plate. Appendix D shows the temperature of the liquid at different locations across the cooling plate under steady state conditions at a volumetric flow rate of 198 ml/min. Analysis of Figure 37 indicates that the temperature of the right hand side of the cooling plate is lower than the left hand side by less than one degree at both the inlet end and the outlet end of the cooling plate. This suggests good flow distribution within the cooling plate.

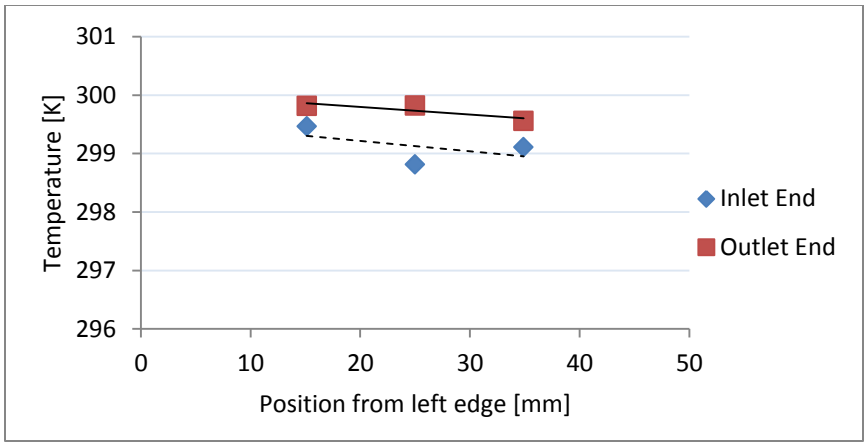

Figure 36: Average temperature of liquid at different locations on cooling plate

6. Conclusions

In this thesis, a thermal management system (TMS) consisting of a series of cooling plates joined to two fluidic headers was designed using 6061 aluminum to remove the heat generated by the adsorption of hydrogen gas within a modular adsorption-based hydrogen storage system. Finite element and computational fluid dynamics analyses were used to size the cooling plates for hydrogen pressure and liquid nitrogen flow rate conditions. Size and weight estimates show a 37.4% decrease in the displacement volume and 80.7% decrease in the weight of the thermal management system when compared with prior efforts to store 5.6 kg of hydrogen using a stainless steel TMS. Further, a manufacturing plan was proposed consisting of photochemical machining and laser welding of aluminum cooling plates followed by vacuum brazing of the cooling plates onto fluidic headers and precipitation hardening heat treatment. As reported in prior work [41], estimates for the total unit production cost are $279.36 per system based on a production volume of 500,000 units.

In order to demonstrate feasibility of the system design and manufacturing plan, several aluminum cooling plates were successfully welded using a full penetration (750 μm deep) laser weld with a power of 500 W at a speed of 180 mm/s. The aluminum was quenched from solution heat treatment conditions in air under equilibrium conditions. Under these conditions, weld joint strength was found to be approximately 67% of the base material strength. Weld fracture surfaces predominately showed evidence of ductile behavior though some solidification cracking was found. Although cross-sections of weldments showed high levels of porosity, all cooling plates were found to be hermetic up to 100 psi.

Warpage of the cooling plates was analyzed after different fabrication process steps to assess the ability to hold microchannel dimensions. It was found that laser welding induced a higher amount of warpage in the cooling plates compared to solution heat treatment and quenching in air by free convection. The warpage in the cooling plates was found to be less than one percent of the overall adsorption bed height. Variations in microchannel heights were approximately 4% across the plate which is suitable for microchannel arrays. Microchannel variation was dominated by photochemical etching and not the bonding step.

Finally, the fabricated cooling plate was tested to evaluate the cooling capacity, flow distribution and the pressure drop through the cooling plates. At the designed volumetric flow rate of 50 ml/min of water, the device removed 86.6% of the required heat load of 22.4 W with a pressure drop of less than 1 atm and good thermal distribution along the top surface of the cooling plate. Experimental errors were attributed to heat losses caused by the high thermal conductivity of the aluminum alloy. At 198 ml/min, the cooling capacity error and average pressure drop error values were found to be less than 1% and 10% of CFD simulations, respectively. Collectively, these results suggest that laser welding and heat treatment of a 6061 Al alloy can be used to meet the requirements of a microchannel cooling plate for a thermal management system designed for adsorption-based hydrogen storage systems.

Bibliography

Hydrogen Storage Literature

1. U.S. Department of the Interior, U.S. Geological Survey, World Petroleum Assessment 2000: Description and Results, (2000), http://pubs.usgs.gov/dds/dds-060/
2. Oak Ridge National Laboratory, Transportation Energy Data Book: Edition 25, 2006, "Table 1.13 Consumption of Petroleum by End-Use Sector, 1973-2003," 1-17.
3. U.S. Department of Energy, Energy Information Administration, Annual Energy Outlook 2006: With Projections to 2030, (February 2006), DOE/EIA-0383(2006), http://www.eia.doe.gov/oiaf/archive/aeo05/pdf/0383(2005).pdf.
4. Multi-Year Research, Development and Demonstration Plan, Program benefits 2009
5. U.S. Department of Energy, the Department of Energy Hydrogen and Fuel Cells Program Plan. An integrated strategic plan for the research, development, and demonstration of hydrogen and fuel cell technologies, September 2011.
6. "Technology Validation: Fuel Cell Bus Evaluations," DOE Hydrogen Program 2010 Annual Progress Report, http://hydrogen.energy.gov/annual_progress.htmlhttp://hydrogen.energy.gov/pdfs/progress10/viii_7_eudy.pdf
7. DOE Hydrogen and Fuel Cells Program Record #10001, http://hydrogen.energy.gov/program_records.html.

8. DOE 2011 Interim Update Technical Plan — Storage, http://www1.eere.energy.gov/hydrogenandfuelcells/mypp/pdfs/storage.pdf
9. Li Zhou, “Progress and problems in hydrogen storage methods”, Renewable and Sustainable Energy Reviews, vol. 9, pp. 395–408, 2005
10. Andreas Zuttel, “Hydrogen storage methods”,Springer-Verlag, pp. 157-172, 17 March 2004
11. "Targets for Onboard Hydrogen Storage Systems for Light-Duty Vehicles," U.S. Department of Energy, Office of Energy Efficiency and Renewable Energy, [Online]. Available: http://www1.eere.energy.gov/hydrogenandfuelcells/storage/pdfs/targets_onboard_hydro_storage_explanation.pdf.
12. J. Zhang and T. Fisher, "A Review of Heat Transfer Issues in Hydrogen Storage Technologies," Journal of Heat Transfer, vol. 127, pp. 1391-1399, 2005.
13. T. Hua, R. Ahluwalia, J. Peng, M. Kromer, S. Lasher, K. McKenney, K. Law and J. Sinha, "Technical assessment of compressed hydrogen storage tank systems for automotive applications," International Journal of Hydrogen Energy, vol. 36, pp. 3037-3049, 2011.
14. R.K. Ahluwalia, T.Q. Hua, J.K. Peng, “On-board and Off-board performance of hydrogen storage options for light-duty vehicles”, International Journal of Hydrogen Energy, vol. 37, pp. 2891-2910
15. A. Zuttel, "Materials for hydrogen storage," Materials Today, pp. 24-33, September 2003.

16. C.R. Baker, R.L. Shaner, “A study of the efficiency of hydrogen liquefaction” , International Journal of Hydrogen Energy, Volume 3, Issue 3, Pages 321–334, 1978.
17. Li Zhoua, Yaping Zhoub, Yan Suna, “Enhanced storage of hydrogen at the temperature of liquid nitrogen”, International Journal of Hydrogen Energy, vol. 29, pp. 319 – 322, 2004.
18. R. Ahluwalia, T. Hua, J. Peng, S. Lasher, K. McKenney, J. Sinha and M. Gardiner, "Technical assessment of cryo-compressed hydrogen storage tank systems for automotive applications," International Journal of Hydrogen Energy, vol. 35, pp. 4171-4184, 2010.
19. Weidenthaler, C. and Felderhoff, M., "Solid-state hydrogen storage for mobile applications: Quo Vadis?," Energy & Environmental Science, vol. 4, pp. 2495-2502, 2011.
20. B. Sakintuna, F. Lamari-Darkrim and M. Hirscher, "Metal hydride materials for solid hydrogen storage: A review," International Journal of Hydrogen Energy, vol. 32, pp. 1121-1140, 2007.
21. G. Mohan, M. Prakash Maiya, S. Srinivasa Murthy, “Performance simulation of metal hydride hydrogen storage device with embedded filters and heat exchanger tubes”, International Journal of Hydrogen Energy, vol. 32, issue 18, pp. 4978-4987, 2007.
22. R. Ahluwalia and J. Peng, "Automotive hydrogen storage system using cryo-adsorption on activated carbons," International Journal of Hydrogen Energy, vol. 34, pp. 5476-5487, 2009.

23. M. Niemann, S. Srinivasan, A. Phani, A. Kumar, D. Goswami and E. Stefanakos, "Nanomaterials for Hydrogen Storage Applications: A Review," Journal of Nanomaterials, no. 950967, pp. 1-9, 2008.
24. P. Benard, R. Chahine, P. Chandonia, D. Cossement, G. Dorval-Douville, L. Lafi, P. Lachance, R. Paggiaro and E. Poirier, "Comparison of hydrogen adsorption on nanoporous materials," Journal of Alloys and Compounds, Vols. 446-447, pp. 380-384, 2007.
25. J. Sculley, D. Yuan and H. Zhou, "The current status of hydrogen storage in metal-organic frameworks - updated," Energy & Environmental Science, vol. 4, pp. 2721-2735, 2011.
26. S. Han, H. Furukawa, O. Yaghi and W. Goddard III, "Covalent Organic Frameworks as Exceptional Hydrogen Storage Materials," Journal of the American Chemical Society, vol. 130, no. 35, pp. 11580-11581, 2008.
27. H. Dhaou, A. Souahlia, S. Mellouli, F. Askri, A. Jemni, S. Ben Nasrallah, “Experimental study of a metal hydride vessel based on a finned spiral heat exchanger”, Int. J. Hydrogen Energ. 35 (2010) 1674–1680.
28. F. Laurencelle, J. Goyette, Simulation of heat transfer in a metal hydride reactor with aluminum foam, International Journal of Hydrogen Energy. 32 (2007) 2957–2964.
29. T. Pourpoint, V. Velagapudi, I. Mudawar, Y. Zheng, T. Fisher, Active cooling of a metal hydride system for hydrogen storage, Int. J. Heat Mass Transfer 53 (2010) 1326–1332

30. D. Mori, K. Hirose, Recent challenges of hydrogen storage technologies for fuel cell vehicles, Int. J. Hydrogen Energ. 34 (2009) 4569–4574.
31. Souahlia, H. Dhaou, F. Askri, M. Sofiene ,“Experimental and comparative study of metal hydride hydrogen tanks”, International Journal of Hydrogen Energy, vol. 36, issue 20, pp. 12918-12922, 2011
32. Mandhapati Raju, Sudarshan Kumar, “Modeling of a Helical Coil Heat Exchanger for Sodium Alanate Based On-board Hydrogen Storage System”, COMSOL Conference 2010 Boston.
33. M. Visaria and I. Mudawar, "Coiled-tube heat exchanger for High-Pressure Metal Hydride hydrogen storage systems – Part 1. Experimental study," International Journal of Heat and Mass Transfer, vol. 55, pp. 1782-1795, 2012.
34. D.A. Mosher, D.L. Anton, “Design, fabrication and testing of NaAlH4 based hydrogen storage systems”, Journal of Alloys and Compounds, Vols. 446-447, pp. 380-384, 2007.
35. S. Mellouli, H. Dhaou, F. Askri, A. Jemni and S. Nasrallah, "Hydrogen storage in metal hydride tanks equipped with metal foam heat exchanger," International Journal of Hydrogen Energy, vol. 34, pp. 9393-9401, 2009.
36. M. Visaria, I. Mudawar and T. Pourpoint, "Enhanced heat exchanger design for hydrogen storage using high-pressure metal hydride: Part 1. Design methodology and computational results," International Journal of Heat and Mass Transfer, vol. 54, pp. 413-423, 2011.
37. B. K. Paul, “Chapter 2- Dimensional Control in Microlamination”, http://www.ie.orst.edu/~paulbk/research.htm

38. Dr. Issam Mudawar , “Micro-Channel Heat Exchanger for Metal Hydride Hydrogen Storage”, http://www.purdue.edu/discoverypark/energy/assets/pdfs/technologies/TP_19_Micro-Channel%20Heat%20Exchanger%20for%20Metal%20Hydride%20Hydrogen%20Storage.pdf
39. C. Loeb, A. Truszkowska and G. Jovanovic, "Removal of heat from a hydrogen stroage media by a novel microscale-based heat exchanger," in World Hydrogen Energy Conference, Toronto, Canada, 2012.
40. A. Truszkowska and G. Jovanovic, "Temperature Distribution in Activated Carbon Bed During Adsorption of Nitrogen," in American Institute of Chemical Engineeres, Minneapolis, MN, 2011.
41. Leif J. Steigleder, “A Microchannel-Based Thermal Management System for Hydrogen Storage Adsorbent Beds”, thesis, Oregon state university, 2012.
42. B. Paul, "Micro energy and chemical systems and multi-scale fabrication," in Micromanufacturing and Nanotechnology, 1st Ed., vol. 1, Berlin, Germany, Springer-Verlag, 2006, pp. 323-352.
43. Adaptive Control and Repair for Lap Welds of Aluminum Alloy Sheets Based upon In-Process Monitoring
44. ASTM International, “Standard Practice for Heat Treatment of Wrought Aluminum Alloys” B918/B918M-09, April 2009
45. ASM Handbook , "Heat Treating” Volume 4, 1991

Laser Welding Literature

46. Lan Sheng Xie, Y. Sui, “Diffusion Bonding of Aluminum Alloy Using a High-Boiling Liquid Protection” Materials Science Forum, Vols. 551 - 552, pp. 101-104, July 2007
47. Amir A. Shirzadi , “Diffusion Bonding Aluminium Alloys and Composites: New Approaches and Modelling” , Doctor of Philosophy thesis,University of Cambridge, December 1997
48. Kou, S., Welding metallurgy, 2nd edition, Hoboken, N.J., Wiley-Interscience, pp.1-197, 2003
49. X.Cao, W. Wallace, C. Poon, J. Immarigeon, “Research and Progress in Laser Welding of Wrought Aluminum Alloys. I. Laser Welding Processes”, Materials and Manufacturing Processes, Vols. 18(1), pp. 1-22, 2003
50. X.Cao, W. Wallace, C. Poon, J. Immarigeon, “Research in Laser Welding of Wrought Aluminum Alloys. II. Metallurgical Microstructures, Defects, and Mechanical Properties,” Materials and Manufacturing Processes, Vol. 18 (1), pp. 23-49, 2003
51. Steen, W. M., “Laser Material Processing”, London; Dordrecht; Heidelberg; New York: Springer, 2010.
52. Duley, W. W., “Laser Welding”, New York : Wiley, 1999
53. Hirose, A., Kobayashi, K., Yamaoka, H., Kurosawa, N., “Evaluation of properties in laser welds of A6061-T6 aluminium alloy,” Journal of Light Metal Welding & Construction, 37 (9), pp. 1-9, 1999

54. M Katoh, “Factors affecting mechanical properties of laser welded aluminium alloys”, Welding International, Vol 10(10), pp. 771-777, 1996

55. Ramasamy, S; Albright, CE, “CO2 and Nd : YAG laser beam welding of 6111-T4 aluminum alloy for automotive applications”, J LASER APP, 12(3), pp. 101-115, 2000

56. S. Ramasamy and C.E. Albright, "CO2 and Nd-YAG laser beam welding of 5754-O aluminium alloy for automotiveapplications", SCI TEC Weld. Joining, 6(3), pp. 182-190, 2001

57. Zhao, H., White, D. R., DebRoy, T., “Current issues and problems in laser welding of automotive aluminum alloys,” Int. Mater. Rev., 44(6): 238-266, 1999.

58. Guitterez, L. A., Neye, G., Zschech, E., “Microstructure, Hardness Profile and Tensile Strength in Welds of AA6013 T6 Extrusions,” Welding Journal, 75 (4), pp. 115S-121S, 1996

59. Kutsuna, M., Yan, Q. U., “Study on porosity formation in laser welds of aluminium alloys (Report 2). Mechanism of porosity formation by hydrogen and magnesium,” J. Light Met. Weld. Constr., 36 (11), pp. 1-17, 1998

60. Katayama, S, Seto, N, Kim, J D, Matsunawa, A.,“ Formation mechanism and suppression procedure of porosity in high power laser welding of aluminum alloys “

,ICALEO '98: Laser Materials Processing Conference; Orlando, FL; USA; 16-19 Nov. 1998.

61. Naeem, M.; Jessett. R., “Aluminum tailored blank welding with ans without wire feed, using high power continuous wave Nd:YAG laser”, IBEC’98 Proc. Int.

Body Engineering Conf. Exposition: Body Manufacturing Assembly and Advanced Manufacturing, Detroit , pp. 247-255, Sep 1998.

62. Martukanitz. R.P., Smith. D.J., "Laser beam welding of aluminum alloys", Proc. 6th Int. Conf. on Aluminum Weldments, Cleveland, AWS, pp.309-323, 1995
63. Dawes, C., Laser Welding, 1st edition, McGraw-Hill, Inc., pp. 74-76, 1992
64. El-Batahgy and M. Kutsuna, "ArticleLaser Beam Welding of AA5052, AA5083, and AA6061 Aluminum Alloys", Advances in Materials Science and Engineering, Volume 2009 (2009), Article ID 974182, .
65. Kawamoto, "6061-T6 aluminum alloy using YAG laser and filler metal
66. Ramasamy, S., Albright, C. E., 2000, "CO2 and Nd:YAG laser beam welding of 6111-T4 aluminum alloy for automotive applications," J. of Laser Appl., 12 (3), pp. 101-115.
67. Dausinger, F., Rapp, J., Hohenberger, B., Hugel, H, 1997, "Laser Beam Welding Of Aluminum Alloys: State Of The Art And Recent Developments," Proc. Int. Body Engineering Conf. IBEC '97: Advanced Technologies & Processes, Vol. 33, pp. 38-46.
68. Katayama, S., Mizutani, M., 2002, "Laser Weldability of Aluminum Alloys," Trans. JWRI, 31 (2), pp. 147-155.
69. Paleocrassas, A.G, "Feasibility Investigation of Laser Welding Aluminum Alloy 7075-T6 through the use of a 300 W, Single-Mode, Ytterbium Fiber Optic Laser", Master of Science thesis, North Carolina State University, 2005
70. B. Hu, I. Richardson, "Mechanism and possible solution for transverse solidification cracking in laser welding of high strength aluminium alloy"'

Materials Science and Engineering: A, Volume 429, Issues 1–2, Pages 287–29415 August 2006

71. AWS C3.3:2002 - Recommended Practices for the Design, Manufacture, and Examination of Critical Brazed Components, American Welding Society, 2002.
72. ASTM International D1002 – 10, "Standard Test Method for Apparent Shear Strength of Single-Lap-Joint Adhesively Bonded Metal Specimens by Tension Loading (Metal-to-Metal)", October 2010
73. Apostol et.al "Input Parameters Influence on the Residual Stress and Distortions at Laser Welding Using Finite Element Analysis", U.P.B. Sci. Bull., Series D, Vol. 74, Iss. 2, 2012
74. L J Yang, ZM Xiao, "Elastic–plastic modeling of the residual stress caused by welding" , Journal of Materials Processing Technology 48:589–601, (1995)
75. Y. Ueda, NX Ma "Measuring method of threedimensional residual stresses with aid of distribution function of inherent strain", Transactions of JWRI 23(1):71–78, 1994
76. G. A. Moraitis, G. N. Labeas, "Residual stress and distortion calculation of laser beam weelding for aluminum lap joints", Journal of Material Processing Technology, I98, pg-260-269, 2008.
77. J.M. Costa, J.T.B. Pires, et.al, "Residual stresses analysis of ND-YAG laser welded joints" Engineering Failure Analysis, 2009
78. J. Gilbert Kaufman, "Properties of Aluminum Alloys: Tensile, Creep and Fatigue Data at High and Low Temperatures", ASM International, 1999

Appendix

Appendix A: DOE Targets

DOE Targets for Onboard Hydrogen Storage Systems for Light-Duty Vehicles

Table 2 Technical Targets: Onboard Hydrogen Storage Systems

Storage Parameter	Units	2010	2017	Ultimate
System Gravimetric Capacity: Usable, specific-energy from H_2 (net useful energy/max system mass) [a]	kWh/kg (kg H_2/kg system)	1.5 (0.045)	1.8 (0.055)	2.5 (0.075)
System Volumetric Capacity: Usable energy density from H_2 (net useful energy/max system volume)	kWh/L (kg H_2/L system)	0.9 (0.028)	1.3 (0.040)	2.3 (0.070)
Storage System Cost [b]:	$/kWh net ($/kg H_2)	TBD (TBD)	TBD (TBD)	TBD (TBD)
• Fuel cost [c]	$/gge at pump	3-7	2-4	2-4
Durability/Operability:				
• Operating ambient temperature [d]	°C	-30/50 (sun)	-40/60 (sun)	-40/60 (sun)
• Min/max delivery temperature	°C	-40/85	-40/85	-40/85
• Operational cycle life (1/4 tank to full) [e]	Cycles	1000	1500	1500
• Min delivery pressure from storage system; FC= fuel cell, ICE= internal combustion engine	bar (abs)	5 FC/35 ICE	5 FC/35 ICE	3 FC/35 ICE
• Max delivery pressure from storage system[f]	bar (abs)	12 FC/100 ICE	12 FC/100 ICE	12 FC/100 ICE
• Onboard Efficiency	%	90	90	90
• "Well" to Powerplant Efficiency	%	60	60	60
Charging / Discharging Rates:				
• System fill time (5 kg)	min (kg H_2/min)	4.2 (1.2)	3.3 (1.5)	2.5 (2.0)
• Minimum full flow rate	(g/s)/kW	0.02	0.02	0.02
• Start time to full flow (20°C) [g]	s	5	5	5
• Start time to full flow (-20°C) [g]	s	15	15	15
• Transient response 10%-90% and 90% - 0% [h]	s	0.75	0.75	0.75
Fuel Purity (H_2 from storage) [i]:	% H_2	SAE J2719 and ISO/PDTS 14687-2 (99.97% dry basis)		
Environmental Health & Safety:				
• Permeation & leakage [j]	Scc/h			
• Toxicity	-	Meets or exceeds applicable standards		
• Safety	-			
• Loss of useable H_2 [k]	(g/h)/kg H_2 stored	0.1	0.05	0.05

Useful constants: 0.2778 kWh/MJ; 33.3 kWh/kg H_2; 1 kg H_2 ≈ 1 gal gasoline equivalent.

Appendix B: Preliminary Experiments

B1. Laser Welding

The objective of the preliminary experimental study is to evaluate the effect of the welding parameters on the weld joint. The primary objective of the current research is to obtain a set of laser welding parameters to obtain a hermetic joint with high weld strength to join liquid nitrogen cooling plates.

The laser welding parameters in consideration are laser power, laser speed, duty cycle, and use of shield gas. The weld joint parameters resulting from welding are the weld depth resulting in a hermetic joint, weld width and weld strength. In the current research efforts have been concentrated on weld depth and weld strength.

The weld joint needs to have weld depth greater than the thickness of the plate in order to join the two plates with lap joint. Additionally the joint should be free of defects such as pores, voids, solidification cracking which reduces the strength of the joint. Thus, it is necessary to understand the defects and effect of various welding parameters on the defects and investigate and apply methods to reduce the defects.

In the first part of this section, different types of defects are studied by welding two plates using lap joint and cross sectioning the weld joint to observe the defects.

In the second part, methods to reduce the defects and increase the strength of the joint are applied. Use of shielding gas and proper selection of welding parameters reduce the defects such as porosity and cracking. Precipitation hardening heat treatment is performed on the material to increase the strength of the material and the welded joint.

The third part deals with the effect of duty cycle on the weld width and depth. Duty cycle creates pulses of the given power, for example, Figure C1 shows the laser power at 40%, 80% and 100% duty cycle in a particular time span.

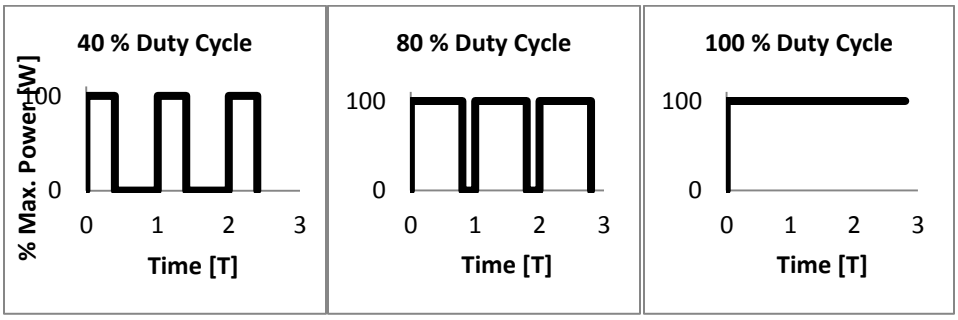

Figure C37: Duty Cycle

B1.1 Experimental Set-up and Protocol

The laser welding experiments were performed on Yb-fibre single mode Rofin laser using the clamp design A shown in Figure 14.

The test articles were cut on shear or on Rofin laser cutting machine and flattened under the pressure of 11 MPa for 15minutes on Vaccum Hot Press. The surface of the samples was roughened using grinding paper and cleaned in an acetone solution prior to welding.

All samples were mounted on the welding clamp design A and the laser head distance was adjusted to obtain the minimum beam diameter at the top of the surface of the material. The laser beam was then defocused 250 μm into the material. Argon was used as a shielding gas whenever required.

For defect analysis and effect of duty cycle analysis the welded samples were mounted in epoxy and cut on the diamond cutter to observe the cross section of the weld. The cross sections were polished on metallographic polishing machine and

etched using hydrofluoric acid to observe the grain boundaries. The cross sections were observed under the microscope for analysis.

For lap shear test, some laser welded samples were heat treated using precipitation hardening process described in Section 3, using water quench. All the samples were tested on Instron Universal Tester at the rate of 0.5mm/s. The weld width and length of the fractured samples at the interface was measured to calculate the strength of the joint.

B1.2 Experimental design and results

B1.2.1. Analysis of Defects

Experiments were conducted on a 0.5 mm thick, 3 cm square test article of 6061-O aluminum alloy. Six lines with different welding parameters were welded on every test article as shown in Figure B2. The design of experiments is shown in Table B1. The laser power and the speed were varied with corresponding duty cycle and all the other laser parameters were kept constant throughout the experiment.

Figure B2: Preliminary Test Article

Table B1: Analysis of Defects Experimental design

Power (W)	Duty Cycle (%)	Speed (mm/s)
400	40	5, 10, 15, 20, 25, 30, 40, 50
500	50	10, 20, 25, 30, 35, 40, 45, 50, 55, 60, 70, 80, 90, 100, 150, 200
600	60	55, 60, 65, 70, 75, 80, 85, 90, 95, 100, 105, 110, 115, 120, 150, 200
700	70	80, 90, 100, 110, 120, 130, 140, 150, 160, 170, 180, 200, 250, 300
800	80	170, 190, 210, 230, 240, 250, 300, 350
900	90	200, 250, 300, 350, 400, 450, 500, 550

The results obtained from the cross section of the weld joint are shown in Figure B3.Figure b3 shows the weld depth and defects at different powers and welding speeds. It can be observed that as the weld speed increases the weld depth decreases and with the increase in the laser power weld depth increases.

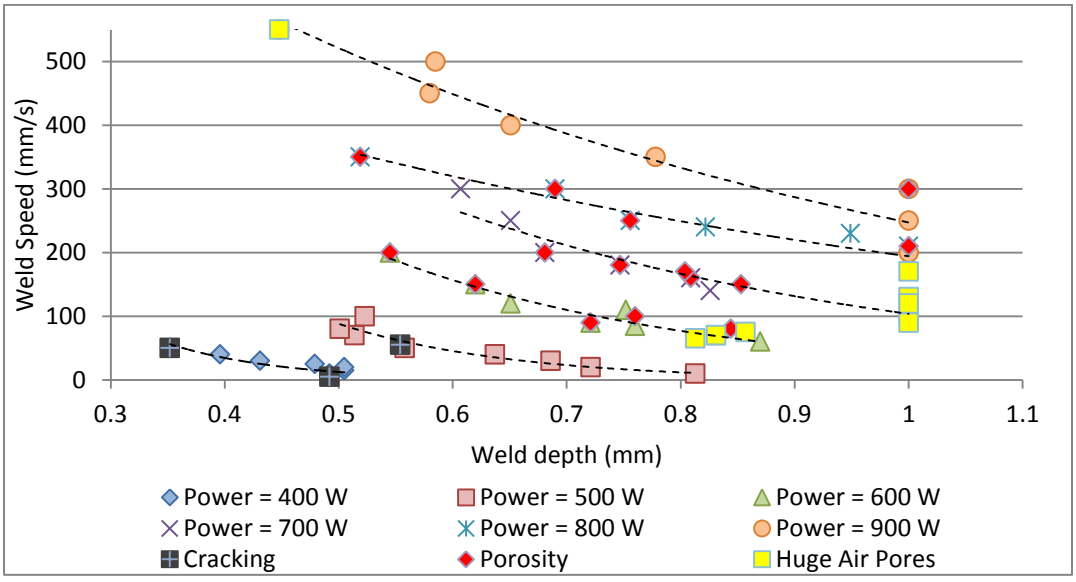

Graph B3: Effect of Power and Speed in weld depth and defects

Four major types of defects observed in the weld joint are cracking, porosity, voids and instabilities (also called humping) as shown in Figure B4.

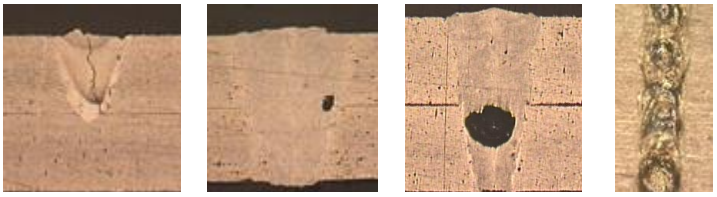

Figure B4: Defects in laser welding (a) Cracking; (b) Porosity; (c) Huge Pores; (d) Instabilities

Porosity and voids are observed in most of the weld joints with no certain pattern. Among the methods reported in the literature, use of shield gas is the most widely used method to reduce the porosity in the weld joint. Shielding gas forms a cover of gas on molten metal to form a barrier between the outer atmospheric air and the molten pool. This reduces the oxidation of metal in the weld joint and formation of air pockets (voids, porosity) due to trapped atmospheric air or hydrogen solubility.

Other defects observed are instabilities or humping forming a discontinuous weld line as shown in Figure B4.Another defect observed is ablation of material at the point where the laser welds initiates and underfill at the end of the weld line. These defects can be avoided by using a power ramp at the beginning and end of the weld line.

B1.2.2. Effect of shielding gas and heat treatment on weld strength

Experiments were conducted to evaluate the effect of shielding gas and heat treatment on the strength of the weld joint. Lap shear test articles were designed as shown in Figure 19.

Four parameters having of approximate weld depth of 0.75mm were selected based on the results obtained in the above experiment. Each level (Power, speed and

duty cycle combination) of welding parameter as shown in Table B2 was tested for four combinations of factors, i.e. use of shielding gas (On and Off) and heat treatment (On and Off). Lap shear tests were performed on the samples with 3 replicates for a total of 16 samples per level. A mixed level, full factorial design was generated for the experiments and randomization was incorporated for performing the experiments.

The precipitation hardening heat treatment was performed on Heat treatment-On samples; the detail process is described in section 3 using water quenching.

Table B2: Lap Shear Test welding parameters

Sample No.	Power (W)	Speed (mm/s)	Duty Cycle (%)
1	900	350	90
2	800	240	80
3	600	85	60
4	500	10	50

Statistical analysis was performed using statgraphics software on the obtained results. Figure B5shows the effect of shielding gas and heat treatment on the yield strength in shear and shear tensile strength of the welded joint. A significant increase in the weld joint strength was observed due to use of shielding gas and heat treatment.

Use of shield gas reduces the porosity in the weld joint and reduces the oxidation in the weld joint, increasing the strength of the joint. Thus, shielding gas and precipitation hardening heat treatment are used in all the future experiments.

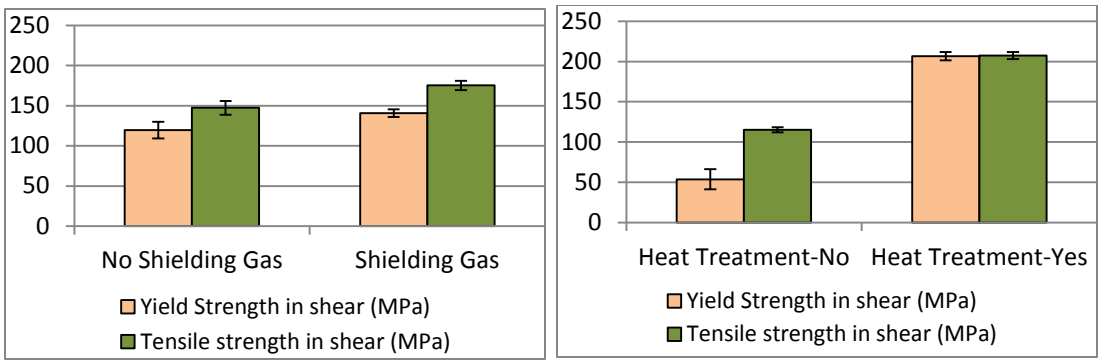

Figure B5: Effect of Shielding Gas and Heat Treatment on Welded Joint Properties

B1.2.3. Effect of duty cycle on weld depth

Experiments were conducted to evaluate the effect of duty cycle on the weld depth. The test article used is 0.5 mm thick, 3 cm square test article as shown in Figure B6. The welding parameters are kept constant including the power and the speed and only the duty cycle is varied. The experimental design is shown in Table B3.

Table B3: Effect of Duty Cycle Experimental Design

Power (W)	Speed (mm/s)	Duty Cycle (%)
900	400	100
900	400	50
900	400	30

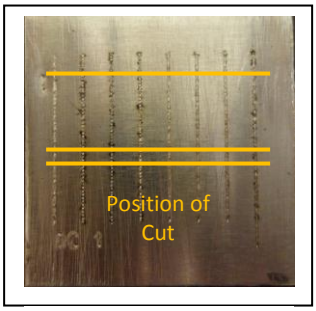

Figure B6: Position of cut of the welded test article

The cross section of the welded joints was observed at three different locations in order to evaluate the effect of duty cycle on weld depth. The welded test article is cut at three different locations at shown in Figure B7

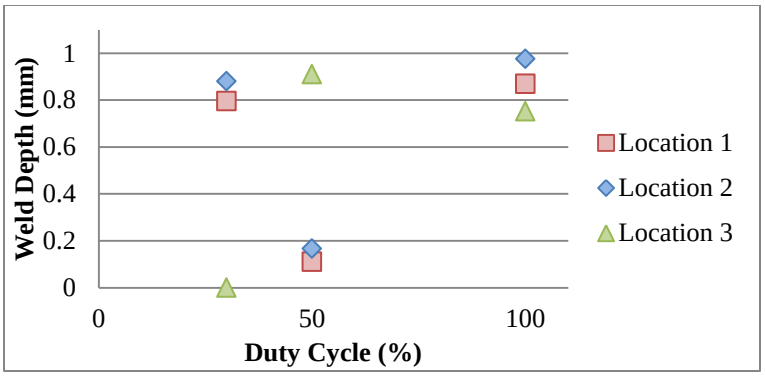

Figure B7: Effect of Duty Cycle on Weld Depth

Figure B7 shows weld depth at different duty cycle and at different location of the weld line. The obtained results shows that the weld depth is not consistent along the weld line, a huge variation in the weld depth is observed with the duty cycle of 30% and 50%. At certain locations the weld depth has not even reached the second shim (>0.5 mm). Weld depth at 100% duty cycle has less variation in the weld depth compared to 30 and 50% duty cycle. The major reason for the variation in the weld depth at 100% duty cycle could be due to the instabilities in the weld line.

Hence, using a lower duty cycle may cause issues like insufficient weld depth leading to non-hermetic seal and lowering the weld strength due insufficient bond area at the interface of the two joining surfaces. Thus it can be concluded that for hermetic applications such as microchannel heat exchangers duty cycle of 100% should be used.

B1.2.4. Parameter Selection

Based upon the results obtained in the above experiments, experimental design was created for parameter selection of future experiments. The duty cycle used is

100% and shielding gas is used during welding. The experimental design is shown in Table B4

Table B4: Experimental Design for Parameter Selection

Power (W)	Speed (mm/s)
500	50,100,150,200, 250, 300, 350, 400
600	100, 150, 200, 250, 300, 350, 400, 450
700	100, 150, 200, 250, 300, 350, 400, 450
800	200, 250, 300, 350, 400, 450, 500, 550
900	300, 350, 400, 450, 500, 550, 600, 650
1000	400, 450, 500, 550, 600, 650, 700, 750

Figure B8 shows the weld depth at different powers and speeds and the defects observed in the weld joint. It can be observed that use of shielding gas has reduced the porosity and other defects significantly. Also, use of 100% duty cycle enables to welding at higher welding speed.

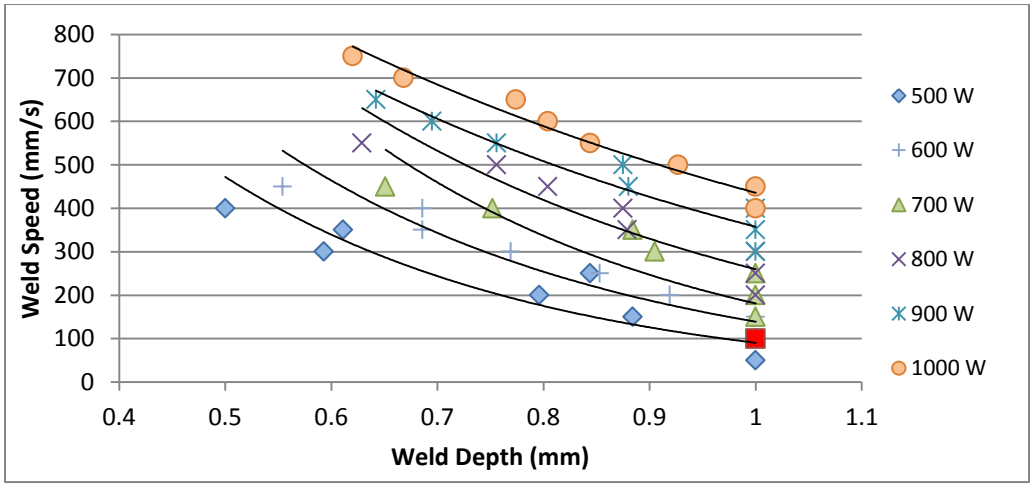

Figure B8: Weld depth and defects at different welding parameters

The requirement of weld depth was considered as 1.5 times the thickness of the shim, which is 0.75 mm in our case. Table B5 shows the parameters that provide the weld depth of approx. 0.75mm.

Table B5: Parameters for lap welding aluminum alloy of 0.5mm thickness

Power (W)	Speed (mm/s)	Weld depth (mm)
1000	650	0.76
900	550	0.756
800	500	0.756
700	400	0.752
600	300	0.787
500	200	0.796

Lap shear test articles were welded and tested using four parameters shown in Table B5 with laser power of 1000 W, 900 W, 600 W and 500 W. Weld joint strength results showed no significant difference in the joint strength of the welded joints when welding at high power condition or low power condition as shown in Figure B9.

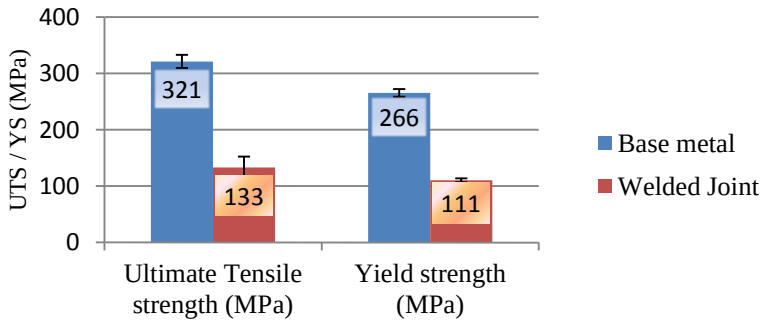

Figure B9: Base metal and weld strength properties for air quench by free convection

B2. Warpage due to heat treatment:

Experiments were conducted to investigate methods to reduce warpage due to heat treatment. Test article used in the current experiment is a 5.5 cm square shims with 0.5 mm thickness. The effect of different quench media is investigated on the warpage of the shim.

The material was annealed and flattened prior to heat treatment in order to remove residual stresses and obtain a flat surface. The shims were solution heat treated at 565 °C for 40 minutes and quenched in different media. Water, ethylene glycol and air were used as the quench media in the current investigation. In the case of the air quenching, the test coupon was allowed to cool by free convection in the ambient environment under equilibrium conditions. The shims were then subjected to aging process at 160 °C for 18 hours.

The warpage in the shims was measured after aging process using ZeScope. The procedure of measurement is explained in Section 5.2. The height of the shim was measured at 36 different locations as shown in Figure B10 below.

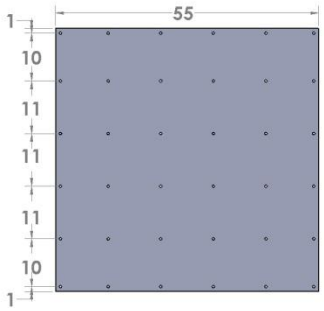

Figure B10: Location of height measurement on the test article

Figure B11 shows the average height of the shim for different quench media and the coefficient of variation of the height. The warpage in water quenched shims is the

highest and the air quenched shims show the lowest warpage. The coefficient of variation air quenched shims is also the lowest compared to the other quench media.

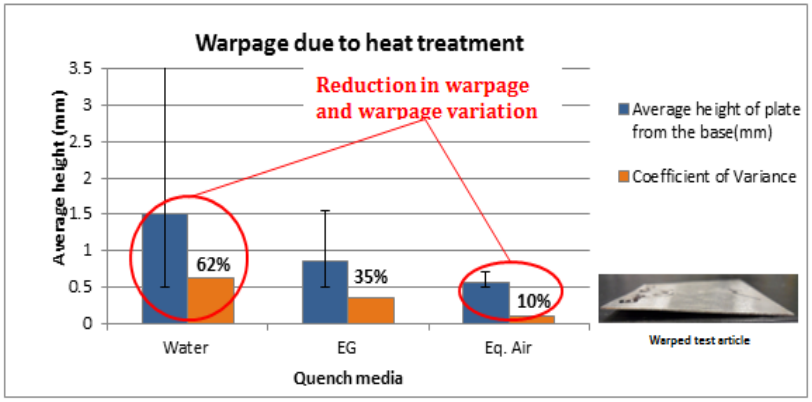

Figure C11: Effect of different quench media on warpage of the shim.

The strength of the base metal test articles was investigated for water quenched shims and air quenched shims using Instron universal tester. Results showed in figure B12 shows no significant decrease in the yield strength of the material using different quench media, but the ultimate tensile strength of the air quenched material showed a decrease in strength by a small amount.

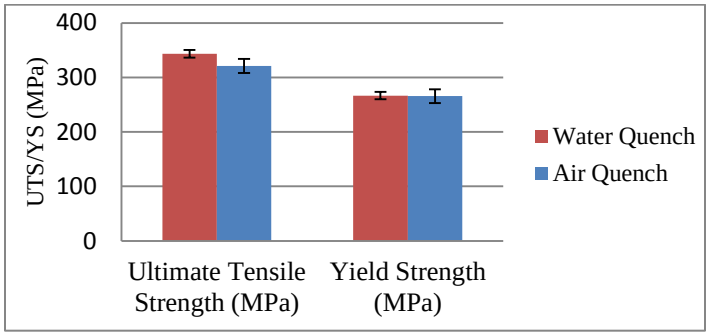

Figure C12: Base metal strength properties for water and air as quench media.

Water provided the highest cooling rate and hence the highest strength is obtained. Ethylene glycol provided slower cooling rates compared to water and hence comparatively lower strengths and lower warpage. Ethylene glycol and oil are generally recommended quench media when warpage of the material needs to be

reduced. Air provided the slowest cooling rate and consequently the lower strengths and warpage.

Thus, in order to reduce the warpage of the shims, air quenching by natural convection should be used. The ASTM standards reported the aging temperature and time based upon the water quenched material. It is necessary to evaluate the peak aging time for air quenched material to obtain the highest strength of the material after aging.

Aging Curve for eq.air quenched 6061 aluminum alloy:

Experiments were conducted to obtain the peak aging time for air quenched aluminum alloy. Standard tensile test coupons were heat treated and quenched in air by free convection. The after quenched samples were then placed in an air furnace for artificial aging at 160 °C. One sample was removed every hour and tested for strength on an Instron universal tester.

The results for the yield strength and ultimate tensile strength for every hour interval is shown in Figure B13. The highest yield strength and ultimate tensile strength of the material is observed at 18 and 20 hours of aging time. Hence, for future experiments aging time of 18 hours is used.

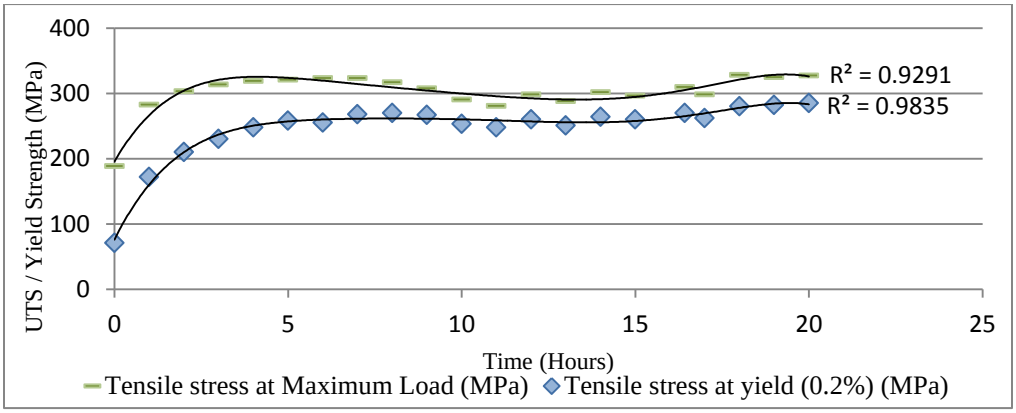

Figure B13: Aging curve for 6061-T6 Aluminum Alloy with air quenching by free convection

B3. Appendix B: Conclusions

Laser welding:

Laser welding parameters performed showed that use of shielding gas and heat treatment increases the strength of the weld joint by reducing the defects and precipitation of hardening elements during heat treatment. Duty cycle of 100% is necessary for application demanding a hermetic seal at the weld joint. Laser welding parameters suitable for welding cooling plates were determined for future primary experiments as shown in table B5

Warpage due to heat treatment:

Heat treatment suitable for the aluminum alloys plates is modified in order to reduce the warpage in the material without reducing the strength of the material considerably. The precipitation hardening heat treatment consists of solution heat treatment of the aluminum alloy at temperature 565 ˚C for 30-40minutes and quenching the material in air by free convection until the material reaches the room temperature. The material is then immediately kept for artificial aging at temperature 160 ˚C for 18 hours. The obtained material after heat treatment is high strength 6061-T6 aluminum alloy.

Appendix C

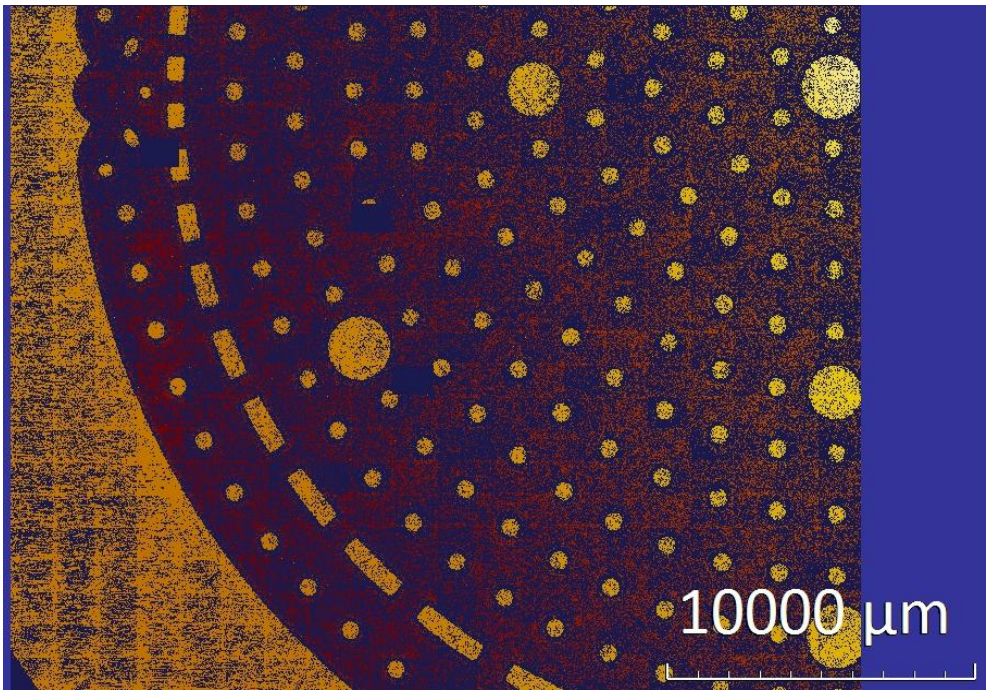

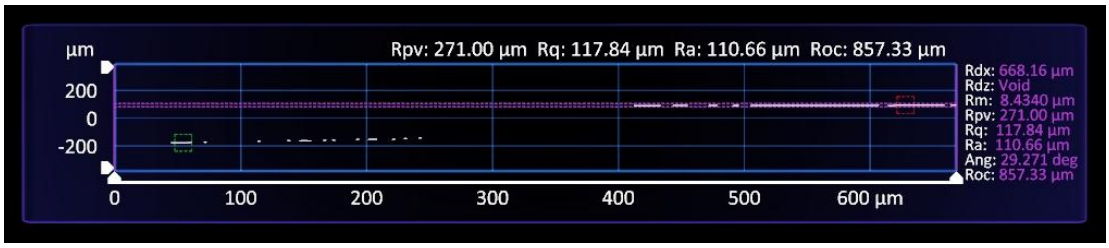

Appendix C top figure shows the quarter profile of the cooling plate etch depth measurement using ZeScope.

Total 55 measurements were taken on the cooling plate. Etch depth of 272.5 µm was obtained with a standard deviation of 4%. Appendix C bottom figure shows the profile of the shim for measurement.

Appendix D

Appendix D shows the temperature of the liquid at different locations across the cooling plate under steady state conditions at a volumetric flow rate of 198 ml/min. Figure D(a) shows the temperature at the center of the cooling plate close to the inlet and the outlet of the plate. It can be observed that the liquid temperature increased from point 2 to point 5, meaning removal of heat from the heat load. Also, temperature at point 4 and 6 are also greater than the temperature at point 1 and 3 showing a heat gain during the flow.

It can be observed from the Figure D(b)that the temperatures at point 4 and 6 are close with a difference in the average temperature of 0.26 K. Similarly, Figure D(c) shows the temperature 1 and 3 are also close with the difference in the average temperature of 0.35 K. This indicates that the flow distribution through the cooling plate is uniform.

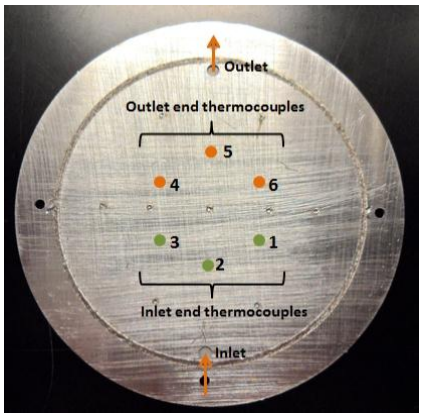

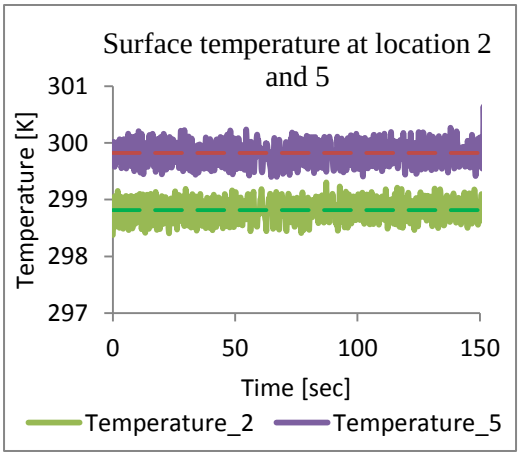

(a)

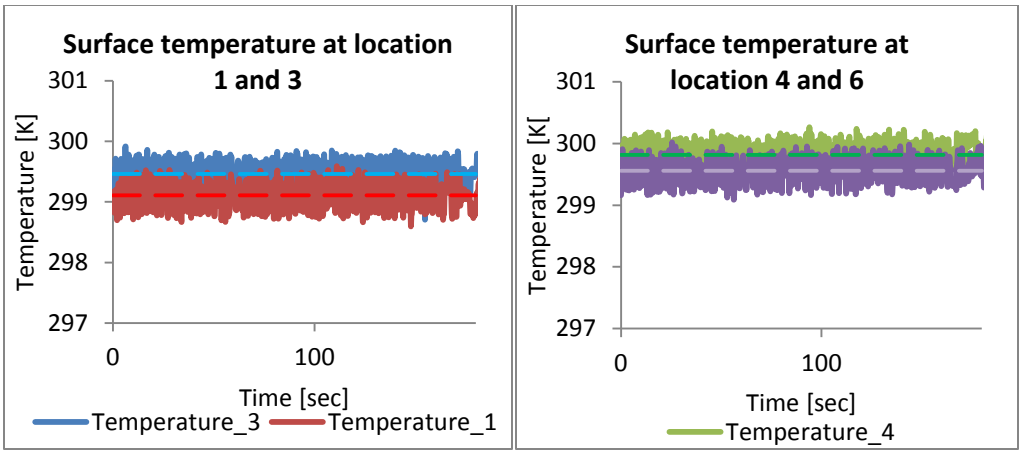

(b) (c)

Figure D: Flow distribution on the cooling plate and liquid inlet and outlet temperature